Technical Report 1630
Vol. 1
November 1993

Radar Detection of Low-Altitude Targets in a Maritime Environment

Final Analysis

Kenneth D. Anderson

Technical Report 1630
Vol. 1
November 1993

Radar Detection of Low-Altitude Targets in a Maritime Environment

Final Analysis

Kenneth D. Anderson

NAVAL COMMAND, CONTROL AND OCEAN SURVEILLANCE CENTER
RDT&E DIVISION
San Diego, California 92152–5001

K. E. EVANS, CAPT, USN
Commanding Officer

R. T. SHEARER
Executive Director

ADMINISTRATIVE INFORMATION

Work for this report was performed by the Tropospheric Branch of the Ocean and Atmospheric Sciences Division. The work was funded by the Office of Naval Research, Arlington, VA.

Released by
R. A. Paulus, Head
Tropospheric Branch

Under authority of
J. H. Richter, Head
Ocean and Atmospheric
Sciences Division

RV

EXECUTIVE SUMMARY

OBJECTIVE

To assess the effects of the evaporation duct on the radar detection of low-altitude, small-radar-cross-section, sea-skimming missile targets.

RESULTS

A unique series of measurements clearly shows that the evaporation duct strongly affects the radar detection of low-altitude targets. Within the horizon, the duct may shift the location of the last interference null several kilometers in range, which may cause nondetection at ranges where detection is expected and detection at ranges where it is not. The evaporation duct may also reduce the signal strength at ranges near the last interference peak such that the detection of a low-altitude target may not be possible until the target is much closer.

At ranges beyond the last optical peak, the radar signal strength depends on both the surface layer and the mixed layer. To accurately model propagation in this region, a knowledge of both surface layer and upper-air meteorology is required. An empirical model to merge the surface layer with the mixed layer has been developed; however, additional studies and measurements are needed to refine this model.

RECOMMENDATIONS

It is strongly recommended that effects from the boundary layer, especially evaporation ducting, be taken into consideration in the design and development of the next generation of radar and close-in weapon systems.

CONTENTS

FIGURES

TABLES

INTRODUCTION

In recent years, instances have been noted when maximum radar detection ranges of low-altitude targets over the ocean are less than expected. These instances of reduced detection ranges are associated with surface-based atmospheric ducting, particularly with evaporation ducting. Effects from these ducts are normally considered to be a long range phenomenon [*Hitney* et al., 1985], but an analysis by *Dockery* [1988a, 1988b] clearly shows reduced detection capabilities for common duct heights, frequencies, and ranges. In addition to the well-known signal enhancement at ranges near and beyond the radio horizon, his modeling indicates that the evaporation duct affects radar detection of small-sized, low-altitude targets within the horizon in two ways: first, it can shift the location of the last optical interference null several kilometers in range, which can cause nondetection at ranges where detection is expected; second, it can substantially decrease signal levels near the last optical interference peak, which may explain the instances of greatly reduced detection ranges.

Figure 1 illustrates these effects on the capability of an X-band radar system that is located 25 m above the sea surface to detect a small target that is located at an altitude of 5 m. Propagation loss (PL), the ratio of transmitted to received power, in dB, versus range, in km, is shown for a family of common evaporation duct heights. The 0-duct-height case corresponds to a standard atmosphere (an atmosphere where the modified refractivity gradient is monotonically increasing at a rate of 0.118 M-units per m), which is the traditional reference in propagation analysis. Assumed radar and target characteristics are such that the radar has a free-space range of 7.5 km (corresponding to a PL detection threshold of 129.3 dB, which is shown as a horizontal broken line in figure 1). When the PL is less than this detection threshold, the radar is able to detect the target; conversely, when the PL is greater than the detection threshold, the radar is not able to detect the target. In a standard atmosphere, the maximum target detection range for this particular radar and target combination is predicted to be 13.5 km. Also, because of the interference between the direct and sea-reflected rays (Lloyd's mirror effect), the target is lost between 6.4 and 8 km by the radar. As atmospheric conditions change from standard to evaporation ducting, PL is predicted to increase at ranges near the last optical interference peak (8 to 13.5 km), to decrease near the last optical interference null location (6.4 to 8 km), and to decrease for ranges beyond the last optical peak. If atmospheric conditions were to change to a 16-m evaporation duct height, the maximum target detection range collapses to 7.5 km—almost half of the range expected in a standard atmosphere.

The significance of this modeling is made evident by figure 2, which shows the worldwide distribution of evaporation duct heights [*Patterson*, 1990]. Approximately 74 percent of the time, the evaporation duct height exceeds 8 m. For the hypothetical X-band radar system used in figure 1, the prediction for an 8-m evaporation duct height is that this radar can just detect a target (5 m above the surface) at a range of 12 km; however, for higher evaporation duct heights, the detection ranges are predicted to collapse back to ranges of about 8 km, or less; therefore, it is predicted that, for about 74 percent of the time, the hypothetical radar detects the target at ranges substantially reduced from the detection range in a standard atmosphere.

An analytical and measurement effort to assess low-altitude, short-range propagation effects at X-band has validated Dockery's modeling. The propagation model used in this analysis combines a radio propagation model, known as Radio Physical Optics (RPO) [*Hitney*, 1992], with atmospheric surface layer models [*Jeske*, 1973; *Liu & Blanc*, 1984; *Paulus*, 1989]. All three featured (enhanced signal beyond the horizon, range shifted null locations, and reduced signal at

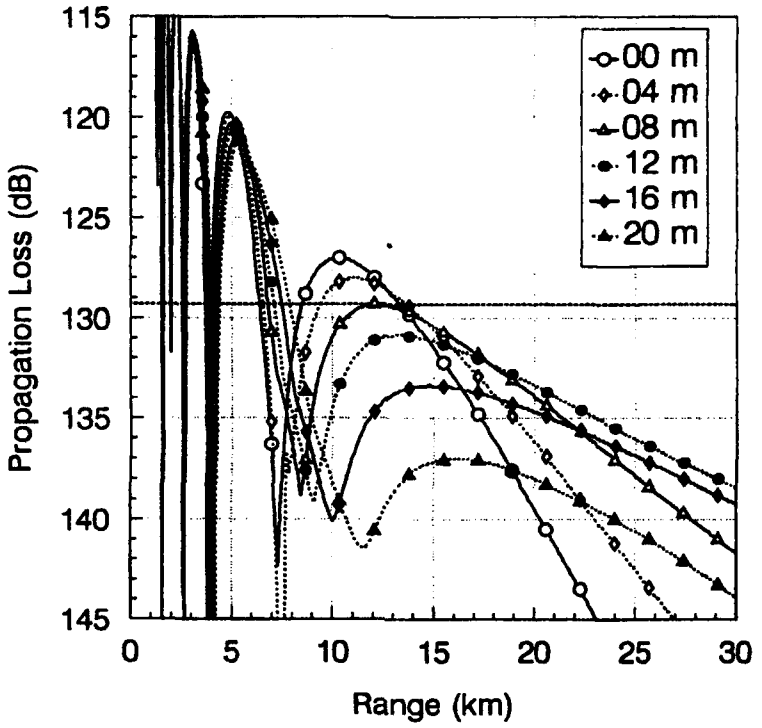

Figure 1. Propagation loss versus range for an X-band radar at 23.5 m above the water, a target at 5 m above the water and parametric in six environmental conditions. The open circle symbol plot corresponds to predictions for a standard atmosphere. The five other symbol plots correspond to evaporation duct conditions where the duct height is 4, 8, 12, 16, and 20 m.

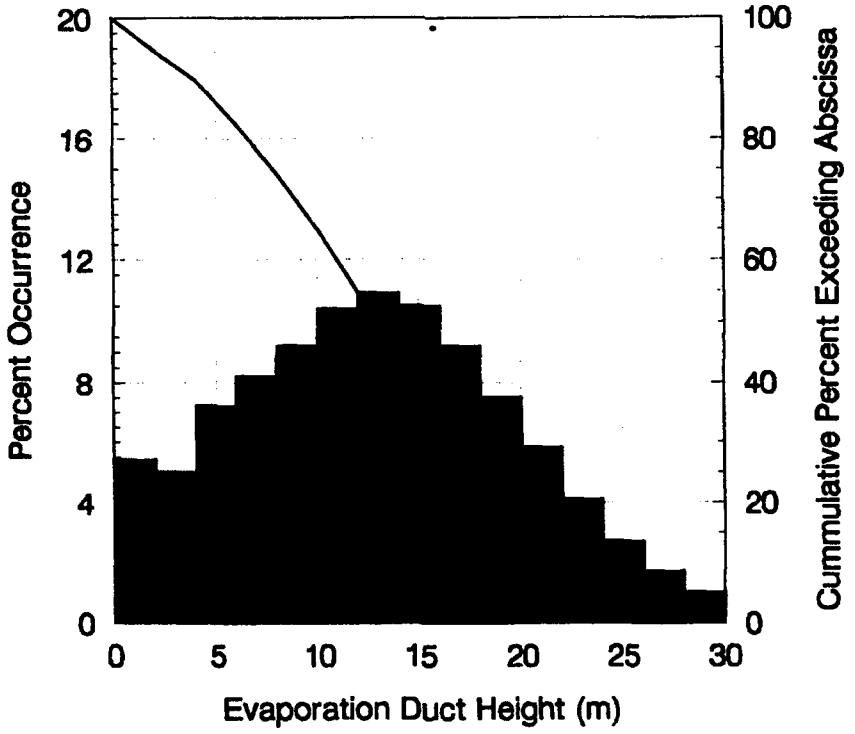

Figure 2. The worldwide distribution of evaporation duct heights (after *Patterson*, 1990).

the last interference peak) have been observed in a carefully controlled radar experiment. Although the essential features are observed in the radar data, discrepancies between the predicted and measured data warrant a closer examination of the meteorological measurements and surface layer theory. New techniques for describing the evaporation ducting environment are discussed. These techniques reduce the discrepancies between the predicted and measured radar data, and they provide valuable insight into the problems associated with measurement of boundary meterological conditions.

The measurement program is reviewed, first as an overview, then as a description of the radar system, targets, and meteorological sensors comprising the experimental measurements. The propagation model is briefly examined to familiarize the reader—details of the individual models are readily available in the literature. Primary results of the measurement program are presented, but not all data are described here. However, a companion report [*Anderson*, 1993] documents all radio and meteorological data. Finally, the results are summarized, conclusions are drawn, and recommendations are made.

MEASUREMENT PROGRAM

A measurement program to validate the predicted propagation effects was started in June of 1989. To represent typical shipboard radars, an X-band radar, operating at a frequency of 9.415 GHz, was placed 23.5 m above mean sea level (msl) on a site at the Naval Command, Control and Ocean Surveillance Center RDT&E Division (NRaD), San Diego, California. The radar site is commonly known as the F35 site. Figure 3 is a geographical map of the test area, and it shows range rings in 25-km intervals about the F35 site. The site is ideal because the radar has an unobstructed view of the ocean for azimuths from 180 to 340 degrees. Winds are generally from the northwest, which implies that the local conditions are representative of the sea and not the land. Air temperature, relative humidity, wind speed, and wind direction sensors were mounted on a platform overlooking the ocean approximately 22 m above msl. Sea surface temperature was monitored with two infrared temperature transducers pointed toward the sea surface at zenith angles of approximately 60 and 75 degrees. The infrared spots were in the surf zone and are not considered representative of the sea temperature at ranges beyond 1 km, or so—their primary purpose was to check the consistency of other data.

Under contract to NRaD, a high-speed, ocean-going boat was specially adapted to carry two lightweight corner reflectors of 30-dBsm cross-section. Both were originally mounted 4.9 m above the surface of the ocean, one reflector faced aft and the other faced forward. Later in the measurement program, the aft corner reflector was lowered to a height of 2.6 m to assess height dependencies. Horizontal and vertical beamwidths of the corner reflectors were approximately 40 degrees, which allowed considerable motion of the boat without affecting the cross-section seen by the radar. A radar transponder antenna (omnidirectional) was mounted 4.5 m above the sea surface on the boat. To minimize any interference with the radar return from the corner reflectors, the first return pulse was delayed 6 μsec (0.9 km in range). A second code pulse was delayed 30 μsec from the first pulse to aid in target location. Temperature, humidity, wind speed, and wind direction sensors were mounted on the boat at a height of 2.5 m. Two temperature probes were mounted approximately 20 cm underwater at the stern of the boat to monitor sea temperature. All meteorological sensors were monitored by a computer that sampled the data every 10 seconds and calculated an average value every minute. Upper-air conditions were measured by using Vaisala radiosondes that were launched either from the boat or from the F35 site. Data collected from the radiosondes were stored on a computer.

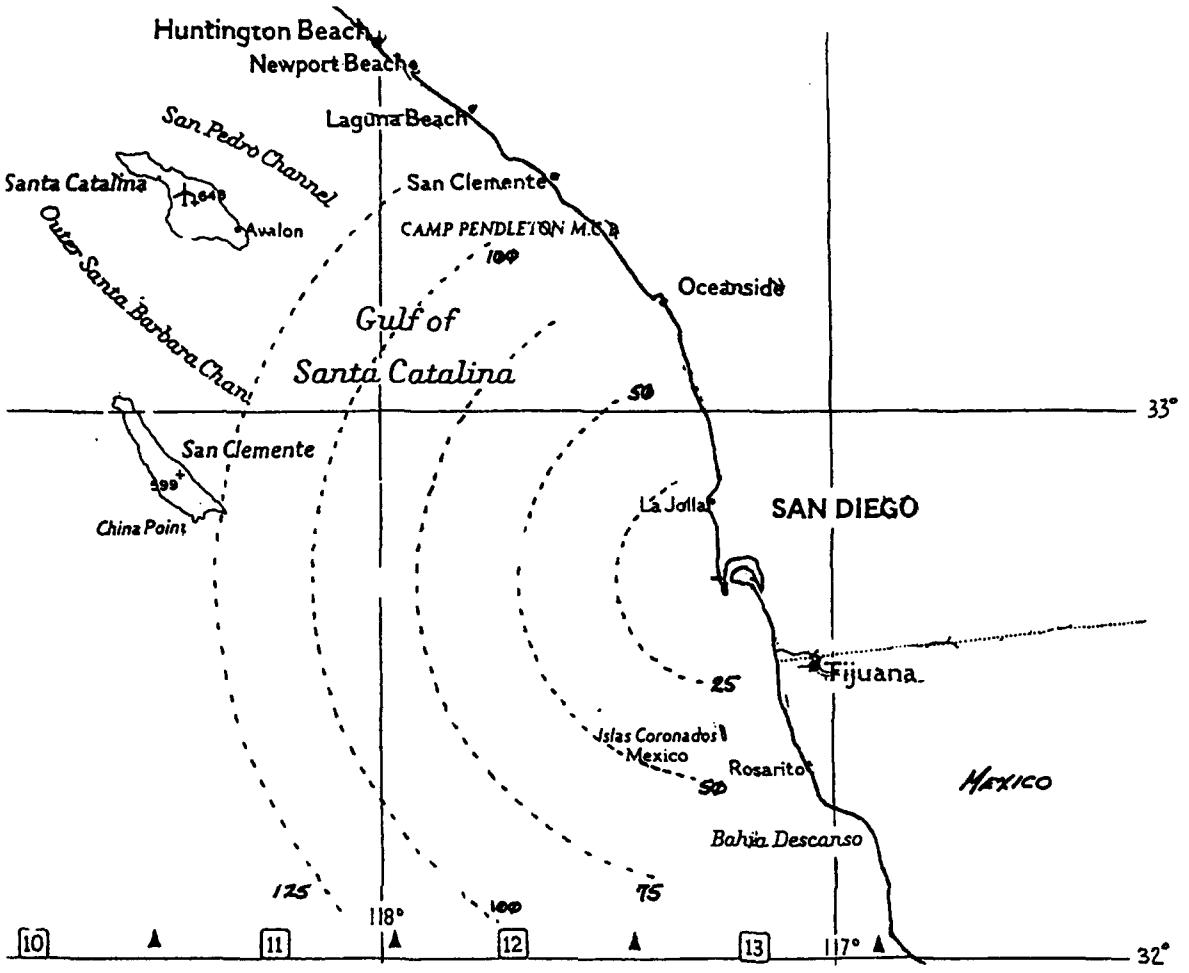

Figure 3. Geographical map of the radar F35 site. The range rings around the radar are distance from the radar in km.

In a typical measurement, the boat was positioned 2 to 3 km seaward from the radar, where the crew made a measurement of the surface meteorological conditions with a set of sensors independent from those sensors monitored by the computer. The crew may also have launched a radiosonde for upper-air analysis. After these measurements were complete, the boat proceeded in a seaward direction, on a radial from the radar, to a range of about 25 km. During this outbound run, radio communication between radar site personnel and boat crew was maintained, either on a VHF or on a UHF link, to provide course corrections. Little or no course correction was ever needed. At the maximum range, the crew made another measurement of the meteorological conditions. For its inbound run, the boat returned on a radial to the starting point. If interesting results or measurement problems arose from the first two runs, the boat would repeat both the outbound and the inbound run, making any additional surface or upper-air measurements. At the F35 site on shore, surface meteorological measurements were made by hand every half hour, or so, depending on conditions. A radiosonde may have been prepared and launched to complement the upper-air observations from the boat.

RADAR, TARGETS, AND METEOROLOGICAL SENSORS

A block diagram of the radar system and test setup on shore is shown in figure 4. Pertinent system parameters are listed in table 1. The radar is a Furuno Model 2050X operating at 9.415 GHz and radiating an average power of 36 W. Radar display circuits were modified to tap off the radar video and timing signals, the scanner timing signal (equivalent to azimuth bearing). A circuit was added for precise gain control. The video signal was routed to a LeCroy, Model 2005, 4-channel, 12-bit A/D waveform digitizer that was controlled by a Compaq 386/20 PC Controller. A special circuit was developed for the PC that combines the scanner and radar trigger timing signals into a trigger signal for the digitizer. Under software control, registers on this circuit were programmed with a starting and an ending azimuth bearing. When the scanner timing signal indicated that the scanner azimuth bearing was between the start and end bearings, the radar triggered the waveform digitizer, causing the digitizer to commence conversions. The digitizer was programmed to take 1024 samples at a 1-MHz rate for each of eight consecutive radar pulses (equivalent to an azimuth sector of 1.9 degrees). Under software control, these 8K samples were transferred to the computer where a 15-km range window (100 samples) was located around the target. The range-gated data from the 1.9-degree sector were further compressed by extracting the maximum signal amplitude for each range bin (150 m) over all eight pulses. The final data were displayed on the screen in an amplitude-versus-range plot (B-scope) for realtime analysis and were written to a disk file for later processing and archiving. Transmitted power was monitored and recorded continuously with a Hewlett-Packard Model 438 power meter.

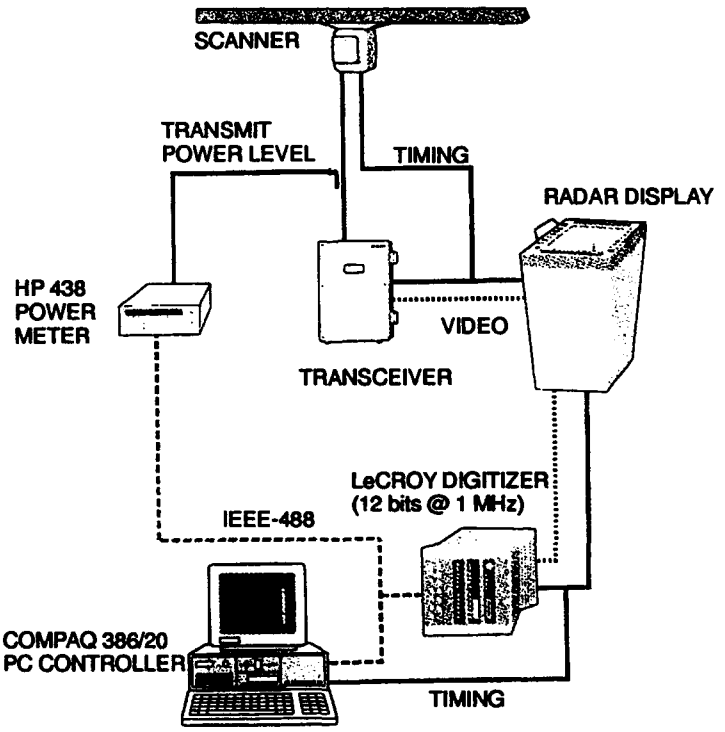

Figure 4. Block diagram of the radar and radar data acquisition system.

A Vega Model 363X transponder was used to calibrate the radar and provide a means for locating the target on the radar display. Table 2 lists the transponder characteristics. Figure 5

shows the calibration plot of the Le Croy digitized output word (plotted as a voltage), in terms of received power at the radar for the gain settings used in the measurements. Each datum on this figure is the median power received for 30 to 50 pulse groups, where each pulse group consists of the maximum signal amplitude for eight consecutive radar pulses.

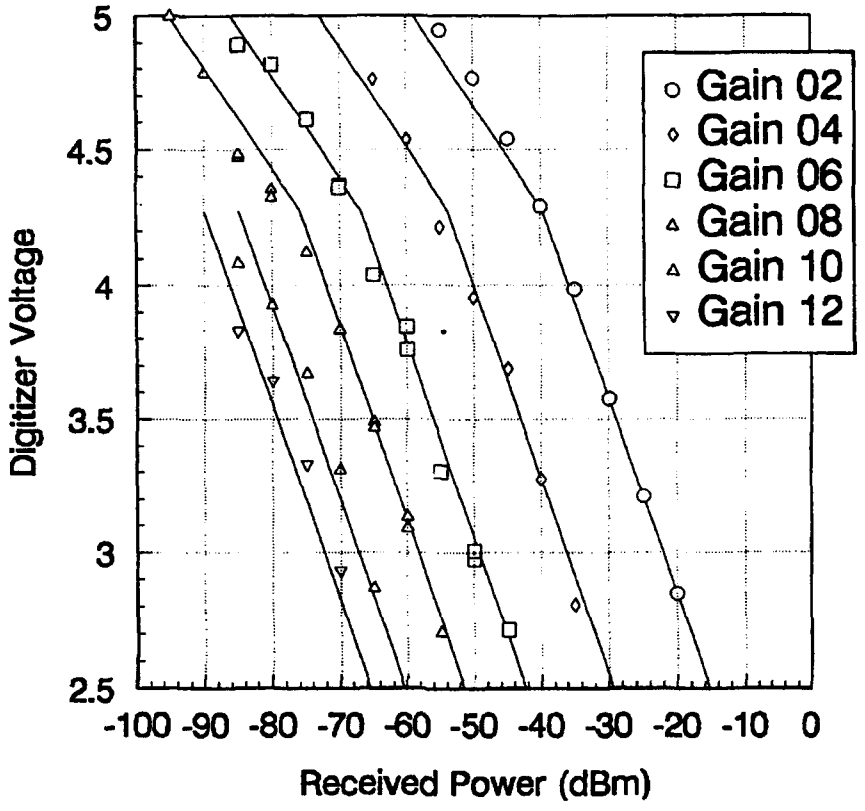

Figure 5. Calibration of the radar system's received power in terms of voltage amplitude at the LeCroy digitizer. The six gain settings are the gains used during the measurements.

The transponder antenna was mounted 4.5 m above the sea surface on the boat. On reception of a radar pulse, the transponder transmitted two framing pulses. The first framing pulse was delayed 6 μs (0.9 km) so it would not interfere with the return from the target. The second framing pulse was delayed 36 μs (5.4 km). On the radar display, these two framing pulses were used as an aid to visually determine the target's actual location in range and bearing.

The targets were Rozendal Associates trihedryal corner reflectors, approximately 1 m on a side. These targets were specially manufactured out of fiberglass to reduce the weight and simplify their installation on the boat. Figures 6 and 7 are the azimuth and elevation patterns, respectively, of one target. The patterns for the second target are nearly identical.

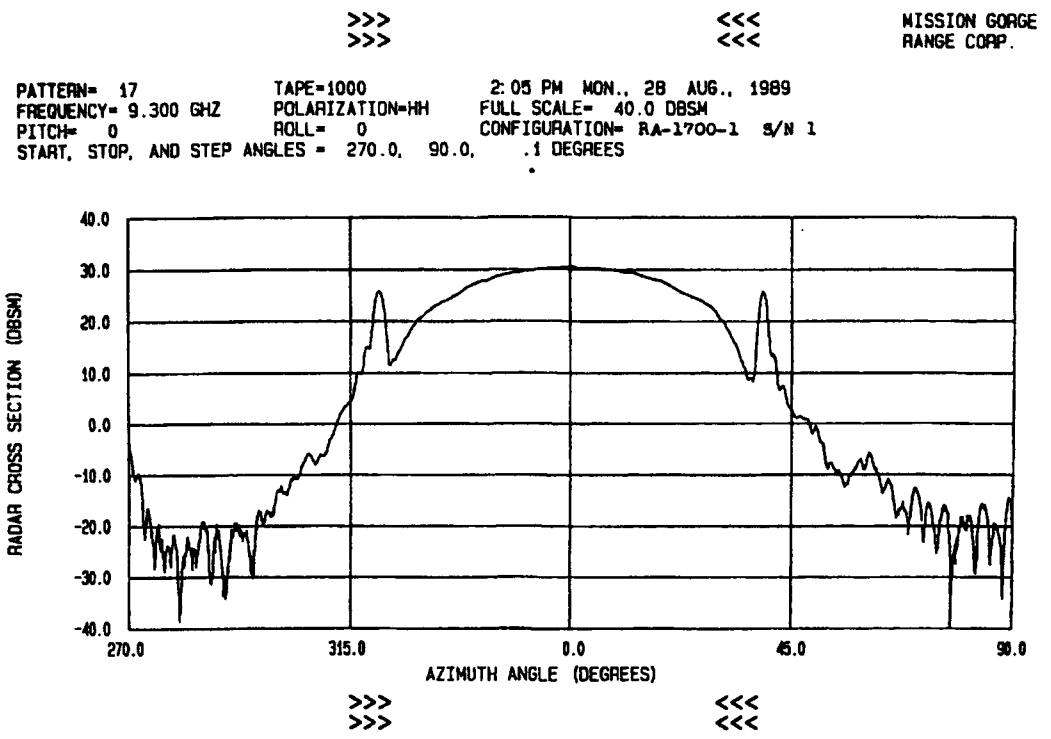

Figure 6. Radar cross-section measurements of a Rozendal Associates trihedryal corner reflector (Serial Number 001) azimuth pattern.

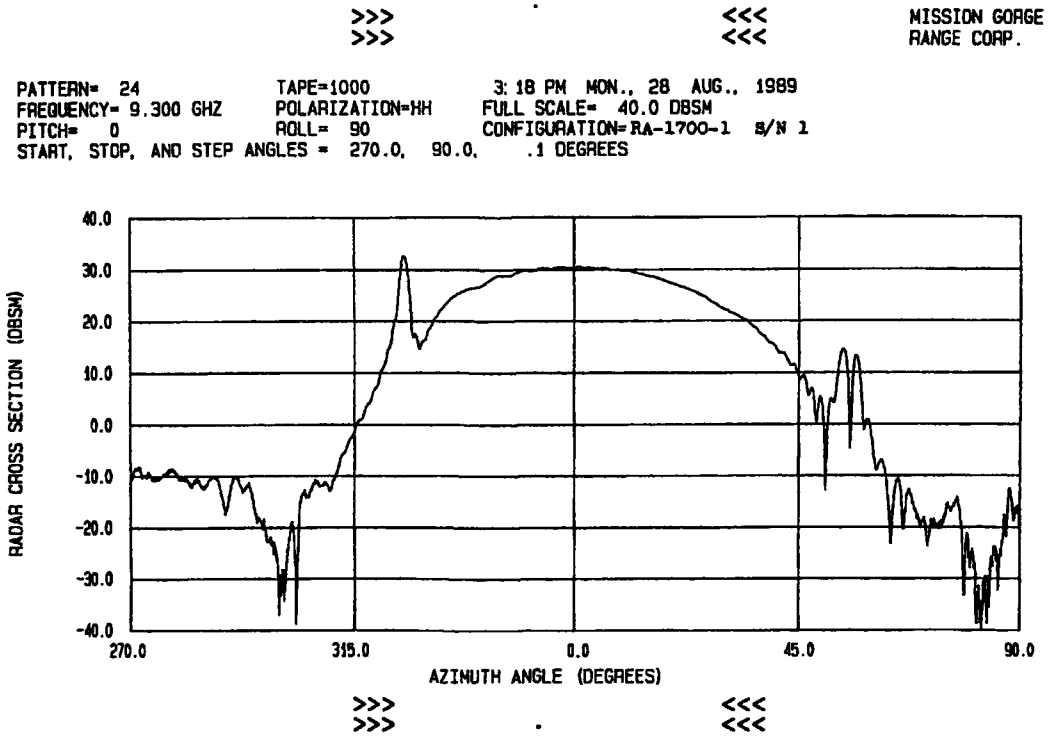

Figure 7. Radar cross-section measurements of a Rozendal Associates trihedryal corner reflector (Serial Number 001) elevation pattern.

Characteristics of the meteorological sensors are listed in table 3. Onboard the boat, a battery-powered microcomputer monitored and recorded wind speed, direction, air temperature, and relative humidity. The data were sampled every 10 s, averaged over a 1-min period, and archived. Sea temperature was logged every minute with two Ryan "Tempmenter" instruments. At the F35 site, a second microcomputer recorded wind speed, direction, air temperature, relative humidity, and sea temperature. As on the boat, these data were sampled every 10 s, averaged over a 1-min period, and archived.

Upper-air measurements were made with Vaisala RS-80 radiosondes launched from both the F35 site and the boat. Typically, the vertical ascent rate of the balloon-borne RS-80 radiosonde was 4 m/s. The data (air temperature T, relative humidity RH, and pressure P) were transmitted to a UHF receiver located near the F35 site. A Vaisala PP-11 processor, connected to the receiver, was used to decode the data as the balloon rose through the atmosphere. Pressure, temperature, and humidity readings from the sensors were transmitted approximately every 1.2 s, which corresponds to a vertical resolution of about 5 m. These data were recorded by a microcomputer and displayed in realtime. An example recording of air temperature and relative humidity versus pressure, for the balloon launch on 11 October 1990, is shown in figure 8.

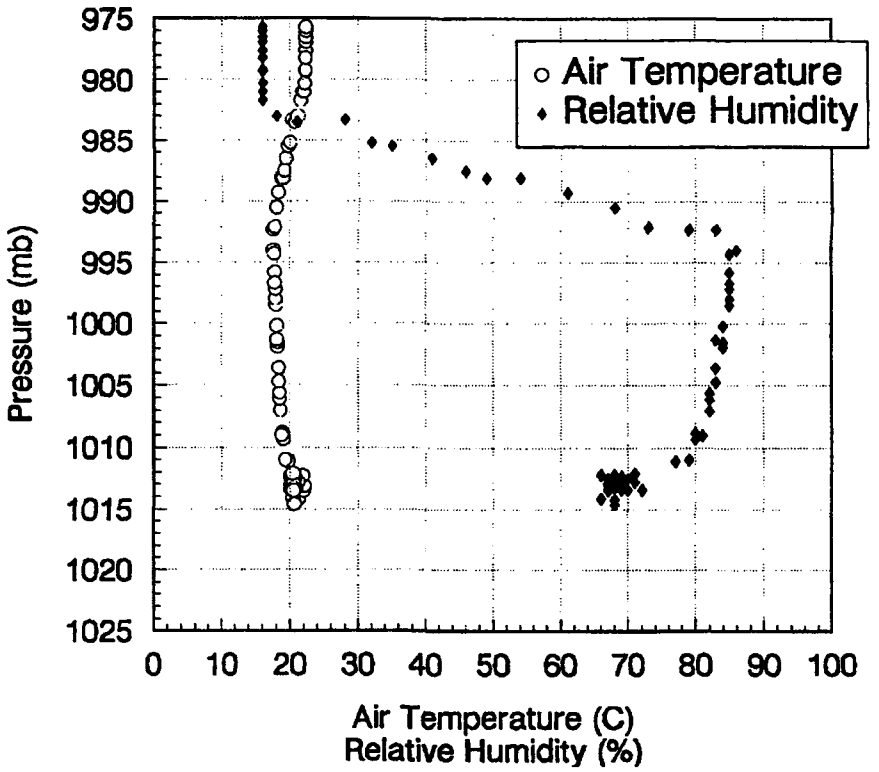

Figure 8. Air temperature and relative humidity versus pressure for the upper air sounding made on 11 October 1990 at 11:54 PDT.

PROPAGATION MODEL

A complete propagation model consists of both meteorological models, to describe the propagation medium and the boundary conditions, and analytical models, to determine the direction and magnitude of radio frequency energy flow in a height-range space.

Meteorological Models

Radio wave propagation in the troposphere is controlled by the spatial distribution of the radio refractive index n, and by the surface characteristics. A numerically convenient term is the refractivity N that is related to the refractive index by $N = (n - 1)\ 10^6$. The refractivity of a parcel of air is

$$N = \frac{77.6}{T} \cdot \left(P + \frac{4810E}{T}\right) \tag{1}$$

where T is the temperature in Kelvin, P is the pressure in mb, and E is the vapor pressure in mb. For a standard atmosphere, the refractivity monotonically decreases with increasing height at a rate of 39 N/km [*Bean & Dutton*, 1966]. By Snell's Law of refractions, a ray (direction of a normal to the wave front) initially launched at an angle parallel to the earth's surface will be refracted downward as it travels in range. The curvature of the ray path is less than the curvature of the earth, so as the ray travels in range, the height of the ray above the surface increases. The modified refractive index M is a mapping of the vertical refractivity from a curved geometry to Cartesian coordinates, and it greatly reduces the computational complexity of radio propagation analysis. It is defined as $M = N + (Z/a)10^6$, where Z is the height above the earth's surface, and a is the earth's radius (6371 km).

In a well-mixed atmosphere, measurements of T, P, and RH are sufficient to compute the refractivity of the air parcel; however, close to the surface, the meteorological measurements are strongly influenced by turbulence. For example, in figure 8, the data between 1015 and 1018 mb show a temperature scatter of about 4 degrees and a humidity scatter of about 10%. The computed scatter in modified refractivity is about 10 M-units. Instead of using the instantaneous measurements of T, P, and RH to characterize the refractivity close to the surface (in the surface layer), the accepted approach is to model the turbulent transport mechanisms and infer the refractivity.

There is no exact definition of surface layer. Qualitatively, it is that part of the atmosphere immediately above the surface where the momentum flux, heat flux, and moisture flux can be considered as constant [*Panofsky & Dutton*, 1983]. In this layer, both mechanical and thermal forcing affect the turbulence and the variation of the mean wind speed, temperature, and humidity. *Monin & Obukhov* [1954] introduced two scaling parameters for velocity and length that are independent of height in the surface layer. The parameters are the friction velocity u_*, and a length L that depends only on the heat flux and the friction velocity.

$$\frac{\partial i}{\partial z} = \frac{S_i}{\varrho \cdot \varkappa \cdot u_* (Z + Z_0)} \Phi \tag{2}$$

where ϱ is the atmospheric density, $\varkappa$ is von Karmen's constant (0.4), u_* is the friction velocity, Z_0 is a surface roughness parameter, and Φ is a stability function. *Jeske* [1973] proposed that Φ take the form of the Monin-Obukhov logarithmic-linear model

$$\Phi = 1 + a\frac{Z}{L'} \tag{3}$$

for stable conditions (air warmer than the sea), and that Φ take the form of the KEYPS relation [*Lumley & Panofsky*, 1964]

$$\Phi^4 - 4\beta\frac{Z}{L'}\Phi^3 = 1 \tag{4}$$

for unstable conditions (air cooler than the sea). In these expressions, a is taken to be 5.2, β is taken to be 4.5, Z_0 is 0.00015 m, and L' is the gradient form of the Monin-Obukhov scaling length corrected for stability. Jeske uses an empirical profile coefficient Γ to relate L' to physical observables of temperature and wind speed

$$L' = \frac{T_a U^2 \Gamma}{g(T_a - T_s)} \tag{5}$$

where T_a is the air temperature in Kelvin, T_s is the sea temperature in Kelvin, g is the acceleration of gravity 9.8 m/s^2, and U is the wind speed in m/s. Taking the conservative property as potential refractivity N_p, the scaling function N_* is

$$N_* = \frac{\varkappa \cdot \Delta N_p}{\ln\left(\frac{Z_1 + Z_0}{Z_0}\right) - \psi} \tag{6}$$

where ΔN_p is the potential refractivity difference between the surface and a reference height, Z_1, in m. The universal stability function ψ is related to Γ through

$$\psi = \int_0^{Z/L} \left[1 - \Phi(\varsigma)\frac{d\varsigma}{\varsigma}\right] \tag{7}$$

The vertical modified refractivity profile is computed as

$$M = 0.125 \cdot Z + \frac{N_*}{\varkappa \cdot \left[\ln\left(\frac{Z + Z_0}{Z_0}\right) - \psi\right]} \tag{8}$$

The surface layer model of *Liu, Katsaros, & Businger* [1979], also referred to as the LKB model, is based on simultaneously solving the diabatic profile equations for velocity, temperature, and humidity given by

$$\frac{T - T_s}{T_*} = \frac{\ln (Z/Z_T) - \psi_T}{1.14 \cdot \varkappa} \tag{9a}$$

$$\frac{Q - Q_s}{Q_*} = \frac{\ln (Z/Z_Q) - \psi_Q}{1.14 \cdot \varkappa} \tag{9b}$$

$$\frac{U - U_s}{U_*} = \frac{\ln (Z/Z_0) - \psi_U}{1.14 \cdot \varkappa} \tag{9c}$$

For unstable conditions the stability functions are

$$\psi_T = \psi_Q = 2 \cdot \ln \frac{1 + (1 - 16Z/L)^{1/2}}{2} \tag{10a}$$

$$\psi_U = 2 \cdot \ln \frac{1 + (1 - 16Z/L)^{1/4}}{2} + \ln \frac{1 + (1 - 16Z/L)^{1/2}}{2} - 2 \cdot \tan^{-1}(1 - 16Z/L)^{1/4} + \frac{\pi}{2} \tag{10b}$$

For stable conditions the stability functions are

$$\psi_T = \psi_Q = \psi_U = -7 \cdot Z/L \tag{10c}$$

The Monin-Obukhov length is

$$L = \frac{(T \cdot (1 + 0.61 \cdot Q) \cdot U_*)^2}{g \cdot k \cdot (T_* \cdot (1 + 0.61 \cdot Q) + 0.61 \cdot T \cdot Q_*)} \tag{11}$$

The surface roughness parameter Z_0 is related to the wind drag coefficient C_D by

$$Z_0 = 10 \cdot \exp^{-1}\left[\frac{\varkappa}{\sqrt{C_D}}\right] \tag{12}$$

where C_D is computed for the wind speed at 10 m which is given by

$$U_{10} = \frac{U_* \cdot \ln\left(\frac{10}{Z_0}\right)}{\varkappa} \tag{13}$$

The remaining unknowns, Z_T and Z_Q, are related to the Reynolds roughness number, which is related to the surface roughness parameter and the friction velocity [*Liu, Katsaros, & Businger,* 1979].

Equations (9) through (13) are solved iteratively to obtain the estimates of the temperature, humidity, and velocity scaling functions. Equation (9) is used to calculate the vertical temperature and humidity profiles, and, with the hydrostatic approximation to allow the calculation of the pressure profile, equation (1) is used to compute the vertical profile of refractivity.

Radio Physical Optics Propagation Model

RPO is a unique hybrid radio propagation model that uses a combination of ray optics (RO) and split-step parabolic equation (PE) methods [*Hitney*, 1992]. Traditional split-step PE methods [*Tappert*, 1977; *Dockery*, 1988b] have large computational requirements (primarily storage and speed) for the geometry, frequency, and antenna beamwidth. The vertical antenna beamwidth (23 degrees) could be reduced by an order of magnitude without significantly affecting the results; however, with RPO, it is possible to rapidly obtain accurate radio propagation results on a microcomputer using the full vertical beamwidth of the antenna. On a 486/50 microcomputer, the computations for a range varying refractive environment, from the surface to a height of 100 m and to 30 km in range, are completed in about 30 seconds. The timing emphasizes the efficiency and capabilities of the RPO radio propagation model.

The ray trajectory angles in the PE region are kept as small as practical to minimize the execution time. A limiting grazing angle for reflected rays Ψ is determined empirically to establish the separation between the RO and PE regions. For angles greater than Ψ, RO techniques that include the magnitude and phase of each ray are used to compute the PL. For angles less than Ψ, PL is computed using the split-step PE with a varying transform size real-valued sine FFT. The transform size never exceeds 1024 points.

Figure 9 shows the propagation loss in a height-range space for the radar operating in a standard refractive environment. The solid line, starting at 0 m in height, at about 5 km in range, and proceeding upward to 100 m, at about 22 km, indicates the separation between the RO and the PE regions. To the left of this line, the calculations are pure ray optics; to the right of this line, the calculations are pure PE—there is no "blending" of the solutions. RPO is designed such that the accuracy of the propagation calculations is better than 0.1 dB in each region. For the target heights of interest (4.9 and 2.6 m), the solutions are of the PE type, for ranges beyond about 6 km. The vertical mesh separation is 86 cm and the range step is 292 m.

The next section will examine the meteorological and radar measurements and will apply the propagation model to assess its accuracy. Two sets of measurements are examined in detail to illustrate both the strength and weakness of the propagation model. The accuracy of the propagation model is examined, by using all applicable sets of measurements, and statistics of the results are presented.

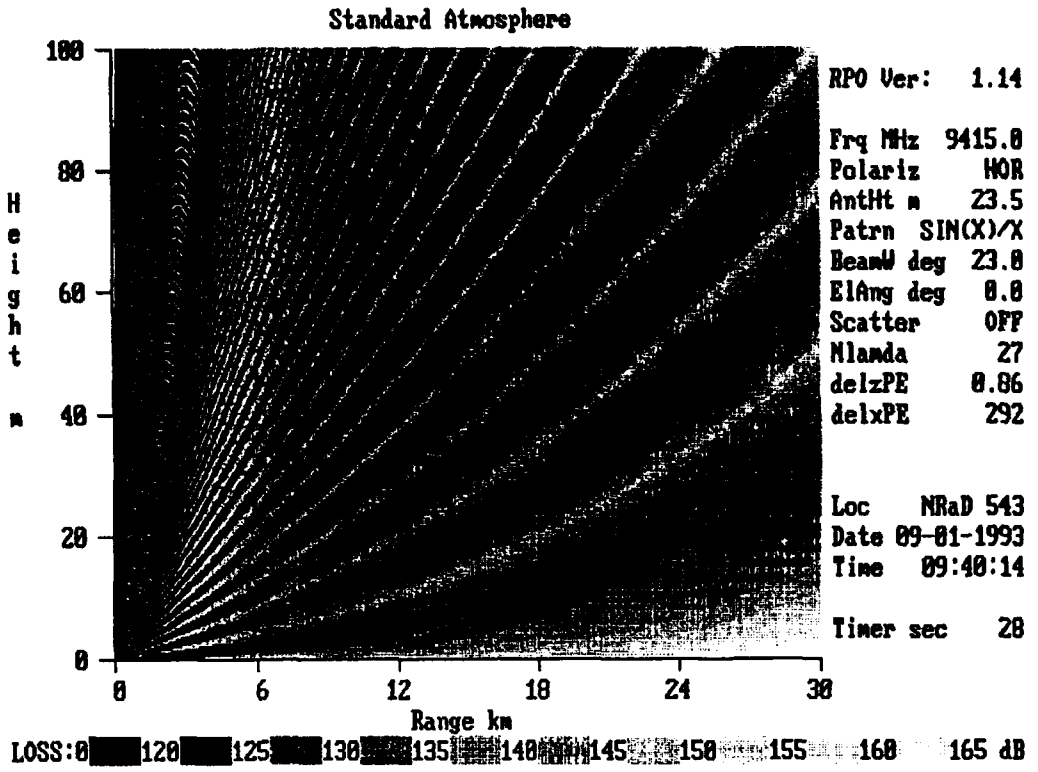

Figure 9. Propagation loss in a height-range space for an X-band radar at 23.5 m above the water in a standard atmosphere. The solid line extending from the surface, at a range of about 5 km to a height of 100 m, is the demarcation between ray-optic and parabolic equation techniques.

RESULTS

Table 4 lists summary information for all 54 sets of measurements. The first set of measurements was made on 11 October 1990; the last set of measurements was made on 14 February 1992. The first column of table 4 is labeled **Seq. No.**, which is used as an abbreviation for Sequence Number. This number, ranging from 1 through 42, is used later in the analysis as a shorthand notation to identify a particular measurement set. The times are local times and they are either Pacific daylight time (PDT) or Pacific standard time (PST), in table 4. The column labeled **Raob Launch Time** is the time identifying not only when a radiosonde was launched, but a particular radiosonde that is thought to best describe the mixed layer refractive gradient. The radar height (in m above the ocean surface) is derived from the median tide height during the measurement period. As mentioned earlier, the target height for both the outbound and inbound boat runs was originally set to 4.9 m. Starting with the outbound run of 1 August 1991, the aft facing corner reflector was lowered to 2.6 m above the water. The rightmost column indicates the dominant refractive condition in the boundary layer. The four conditions are described by three letter abbreviations: first, SBD implies a surface-based duct from an elevated layer; second, NOR signifies a normal or standard atmospheric condition; third, STL is an abbreviation for a surface (or near surface) trapping layer (the question mark on the 6 March 1991 measurements is an expression of uncertainty in the declaration of STL for this day); fourth, ELV indicates an elevated duct. The distribution of refractive conditions is fairly uniform; 15 sets of measurements were made in refractive conditions best described as influenced by an elevated trapping layer; 14 sets were made during both surface-based duct (from elevated layers) and normal (near standard) conditions; and 11 sets were made during refractive conditions dominated by a surface trapping layer.

The effects of the evaporation duct on radar detection range are present in all measurement sets; however, in normal and elevated duct refractive conditions, the effects of the evaporation duct are generally easier to extract from the data. The propagation loss curves shown in figure 1 are for purely evaporation ducting and normal conditions, and it is easy to denote the differences in propagation due to different evaporation ducting conditions. The distinction between evaporation ducting effects and other effects becomes blurred when measurements are made during times that the dominant refractive effects are certain surface-based ducts (from elevated layers) or surface trapping layers. Refractive conditions, where it is strongly felt that the evaporation duct effects could not be readily isolated, were not included in later processing. These measurements sets are indicated by the dash in the **Seq. No.** column of table 4. The meteorological data for these difficult cases is not examined in the current analysis, but is available in the companion data report [*Anderson*, 1993].

The following analysis illustrates the techniques used to develop the statistics of prediction accuracy and shows that the evaporation duct does have a considerable effect on radar detection of low-altitude targets. The problem is to find a meteorological model that best describes the environment in the sense that, for all cases, the predicted propagation loss best agrees with the measured propagation loss.

Without further discussion of why certain treatments were made to specific data, it is best to proceed directly to a detailed examination of several measurement sets, which will lead to an understanding of the techniques used and why some data were deleted from the analysis.

11 OCTOBER 1990

The meteorological and radar measurements for the first measurement period are summarized in figures 10 through 14. The data plotted in these figures are derived from 1-min averages, or the median, in a 1-min time interval of the particular datum.

Figure 10 shows the range from the radar to the boat (in km) and the surface meteorological measurements made on the boat, all plotted versus time. The wind speed (second plot from the top) is linearly interpolated from points in time when the boat was stopped, and the wind velocity was measured by a hand-held anemometer. The relative humidity, air temperature, and sea temperature (from the probes about 20 cm below the surface) are the data recorded by the computer controller. These data are 1-min averages of samples that were taken every 10 s. The humidity and sea temperature traces are reasonably repeatable for both the outbound and the inbound runs, which indicates a range varying meteorological environment and not a temporal varying environment. The air temperature trace, particularly from about 11:15 to 11:30 (PDT), has what appears to be considerable noise superimposed on the trace. The actual meteorological data used in the propagation model were derived from these curves, but with careful analyst interpretation.

Figure 11 is the surface meteorological data recorded at the F35 site (next to the radar). There are two sea temperature traces (from the two IR sensors looking into the surf zone) and an additional plot of wind direction, which can be used to determine if the meteorological measurements at the F35 site are contaminated by air flow from the land.

Figure 12 shows the range from the radar to the boat, the evaporation duct height (calculated from the Jeske method) observed both that the radar site and at the boat, and the air-sea temperature difference, again both at the radar site and at the boat. At the start of the measurements, the boat observations indicate a thermally stable (air warmer than the sea) condition; whereas, the radar site observations indicate a moderate thermally unstable (air cooler than the sea) condition. Shortly after 10:30 (PDT), both the boat, which was proceeding outbound, and the F35 site measurements indicate thermally unstable conditions. At 10:41, the boat proceeded on an outbound run; at 11:03, the boat reached its maximum range (for this run) and additional meteorological measurements were made. At 11:09, the boat began its inbound run and completed this leg at 11:31. The air-sea temperature difference as measured on the boat seems to be fairly repeatable in range, indicating that thermal stability varied more with range than in time. Between 10:30 and 11:30, the wind direction (measured at F35) was fairly consistent in coming from about due south, indicating that the measurements are (probably) representative of over water conditions. The wind speed, measured at F35 was also fairly constant, averaging about 6 knots, over this time interval.

Figure 13 shows the range from the radar to the boat, the azimuth bearing of the boat's position from the radar, the median propagation loss (in dB) between the radar and the boat, the target height above the surface (4.9 m), and finally, the radar height above the water. The slight change in the radar height is due to tidal action. The propagation loss measurements for the last outbound and inbound runs (from about 11:50 to 12:45) are unreliable. Unfortunately, a set of radar control circuits were changed between the first inbound run and the last outbound run and were not recorded in the experiment log book. The "gain" of the radar appears to be about 6 dB higher in the latter measurements, but the actual value of gain or adjustment is unknown and unrecoverable. The last two outbound and inbound runs for this day are not used in the analysis for this reason.

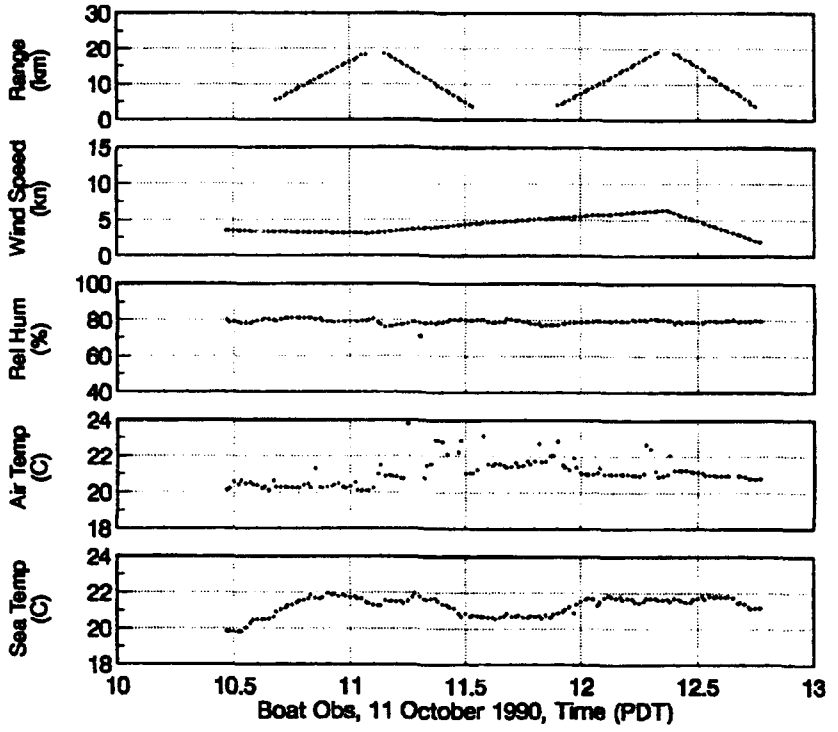

Figure 10. Surface meteorological observations recorded by the sensors on the boat, with the ranges from the boat to the radar, for the measurements on 11 October 1990.

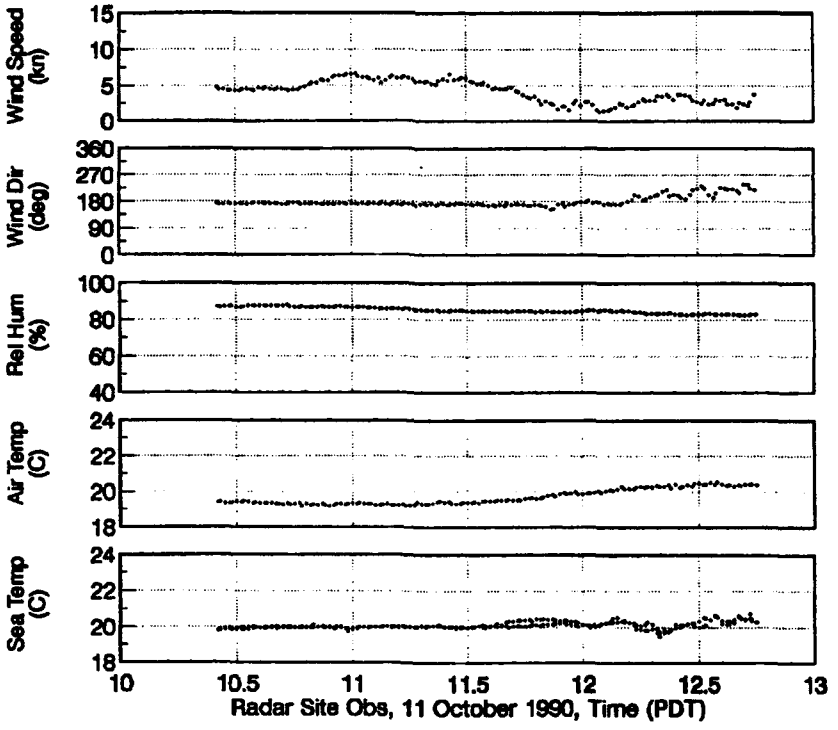

Figure 11. Surface meteorological observations recorded by the sensors on land near the F35 site for the measurements on 11 October 1990.

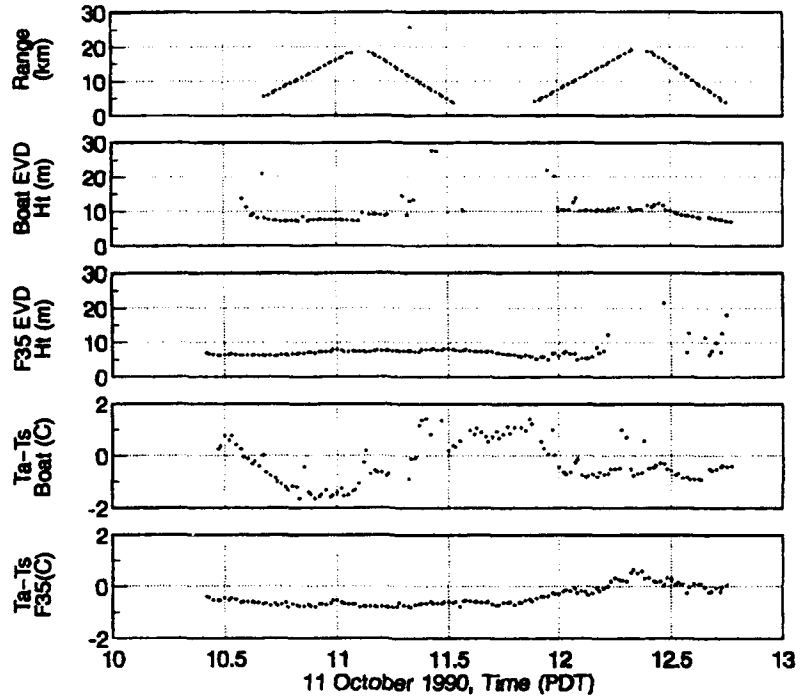

Figure 12. Range from the radar to the boat, evaporation duct heights (Jeske formulation) calculated from surface observations made on the boat and near the radar, and air-sea temperature difference observations made on the boat and near the radar site for 11 October 1990.

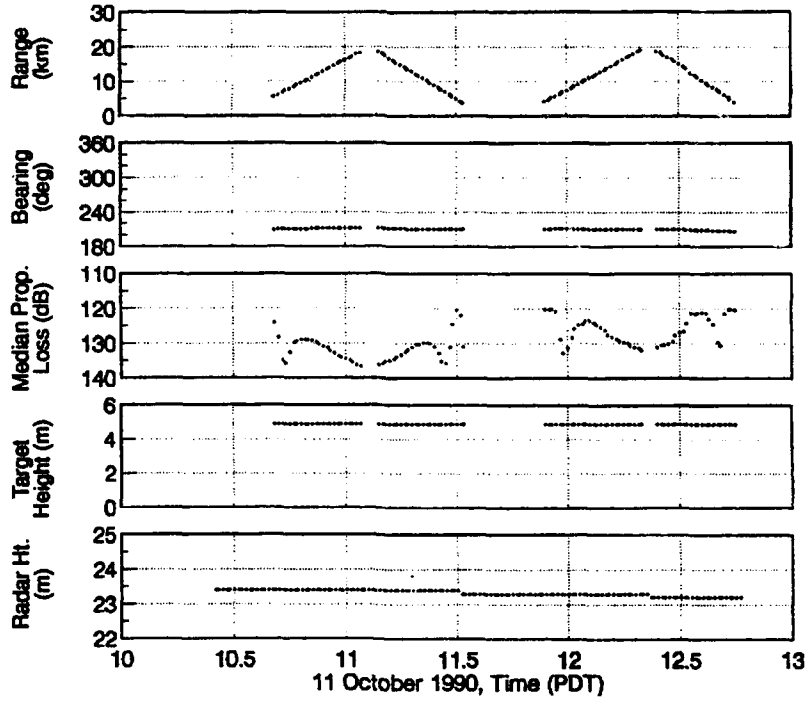

Figure 13. Range from the radar to the boat, azimuth bearing of the boat from the radar, median propagation loss between the radar and the boat, target height on the boat, and the height of the radar above the water for the measurements on 11 October 1990.

Figure 14 is a plot of the modified refractivity (M units) versus height for the radiosonde that was launched at 11:54 (PDT). The launch site was near the radar. Values of M (M is computed using the reported temperature, humidity, and pressure data from the radionsonde) are shown in this figure as open circles. Listed in table 5 is the refractive profile derived from an analyst's interpretation of the data, and it is shown in figure 14 as the solid line. The "bulge" in refractivity near the surface is ignored, as it is thought to be caused by orographic and land-mass heating effects that are probably not representative of conditions over the water. Figure 14 shows a moderate-to-strong surface-based duct from an elevated trapping layer (SBD conditions). The base of the trapping layer is at 197 m, and at this height, it should not have a significant effect on propagation between the radar (height about 23.5 m) and the target (height about 4.9 m) for the ranges of interest.

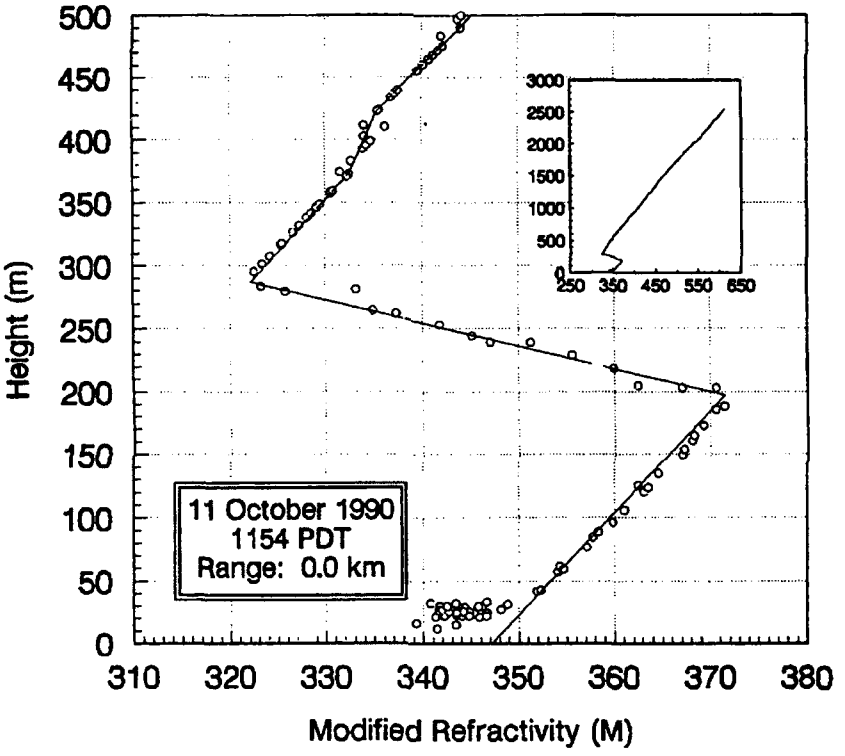

Figure 14. The M profile as measured by the radiosonde launched near the radar site on 11 October 1190 at 11:54 PDT.

Jeske Surface Layer Formulation and Its Variants

The data from table 6 are used to compare the modified refractivity profile using versions of both the Jeske and LKB techniques. Figure 15 shows the comparisons of the measured propagation loss to the results of propagation calculations, using the Jeske and variants of the Jeske formulation. The crosses on this plot indicate the measured propagation loss between the radar and the target. The solid line is the estimate of propagation loss in the presence of a standard atmosphere, and it is included as a reference. At ranges between about 7 through 15 km, the measured propagation loss is consistently greater than the loss predicted for a standard atmosphere. For a propagation loss threshold of 130 dB, the radar is predicted to detect this target at a range of 13.5 km in a standard atmosphere; the measurements indicate that the 130 dB threshold is actually at a range of 11.7 km—about a 10% reduction in detection range. The evaporation duct effect, that of reducing signal strength near the last optical interference peak (at about 9 km in a standard atmosphere), is clearly evident and confirms Dockery's analysis [1988a]. A shift in the last interference null location (at about 7 km in a standard atmosphere), although not as clear as the signal strength reduction, appears to be present, and it lends credence to the validation of the model.

Predictions of propagation loss, calculated using the surface measurements of table 6 and the boundary layer M-unit gradient from table 5, are shown as the four symbol curves on figure 15. The open circle symbol curve is calculated by using the unaltered Jeske formulation (equations [3] through [8]), where the vertical M profile consists of 11-height and M-unit pairs from the surface to a "feature" height and 10-height and M-unit pairs from above the feature height to a height of 100 m. The spacing between height samples is logarithmic. Figure 16 illustrates the shape of the vertical M profiles (unaltered Jeske formulation). The open circle symbols on the M curves correspond to the feature height. For conditions where a minimum on the M profile can be found (the height where a minimum M value can be determined is called the evaporation duct height), the feature height is set equal to the height where M is a minimum. For conditions where an evaporation duct height cannot be determined (e.g., the M profile at 5 km in range in figure 16), the feature height is set to the height of the first valid evaporation duct height in a M profile downrange. If there are no valid evaporation duct heights in downrange profiles, the profiles uprange are examined for a valid evaporation duct height, and the feature height is set to the first valid evaporation duct height found in the uprange profiles. The rationale of a feature height is discussed by *Barrios* [1992].

Returning to figure 15, the propagation loss, predicted by using the unaltered Jeske formulation with the M profiles connected in range through the feature height (open circle symbol), does not agree with the measurements; for example, the predicted location of the last null (about 9 km) does not agree with the observed location of the null (about 7 km); also, the location of the optical peak and the magnitude of the signal are significantly different from the observed. It is strongly believed that the failure to properly predict the measurements is a fault of the meteorological modeling. The arguments to support this belief are developed with the consideration that minor modifications to both the Jeske and the LKB surface layer formulations do not disturb the underlying physics of the modeling. This assumes that the surface meteorological measurements (e.g., table 6) are correct.

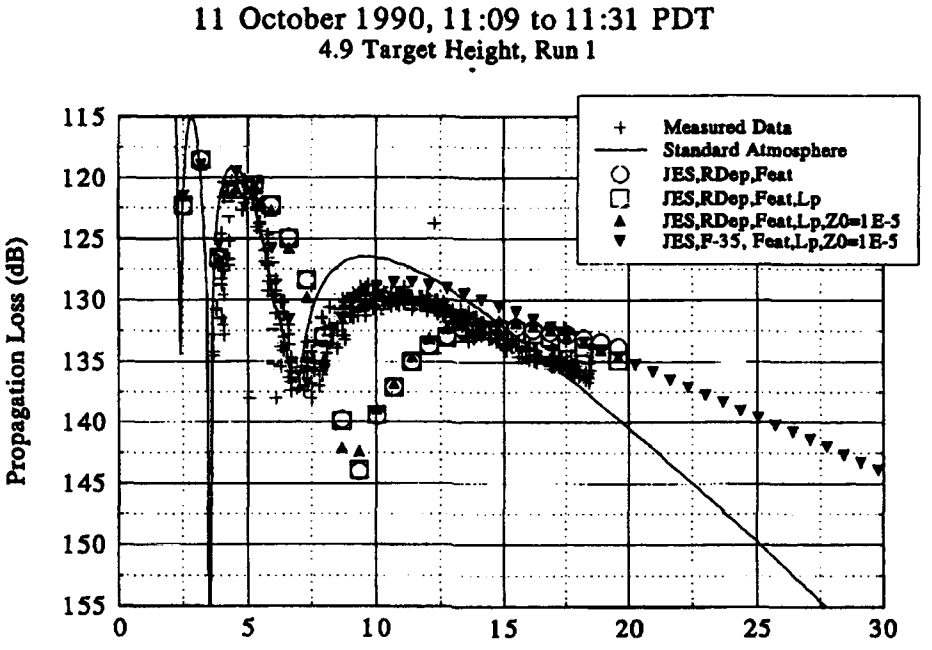

Figure 15. Comparisons of the measured (crosses) to the predicted propagation loss derived from the Jeske (and variants) surface layer model for the run from 11:09 to 11:31 PDT made on 11 October 1990.

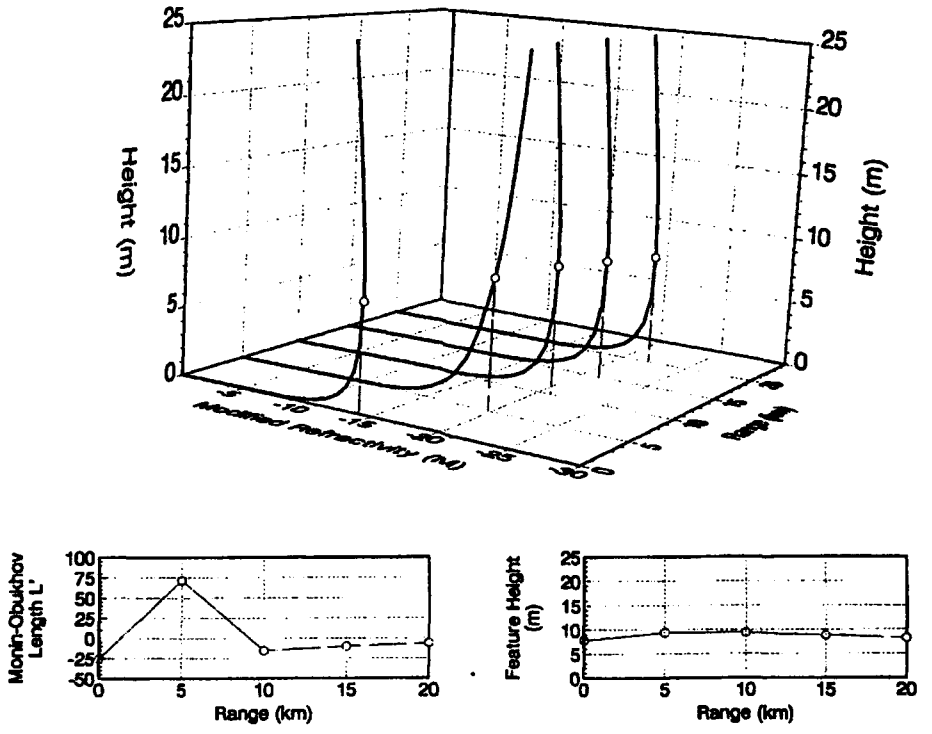

Figure 16. Range dependent height and modified refractivitity profiles derived from the Jeske model for the surface meteorological data listed in table 6.

One such modification forces the M gradient to match the M gradient measured by the radiosonde. Figure 14, the vertical M profile, for 11 October 1990, shows a nearly linear M gradient from a height of about 40 m to a height of about 197 m. In this height interval, the gradient is estimated as 0.1236 M/m. The M profiles calculated from surface layer theory should have this same gradient starting at some height above the surface. One reasonable height, where the gradients can be set equal, is at the height defined by the Monin-Obukhov length L', which can be considered as the height where the inertial force is the same as the buoyancy force. From figure 16, ignoring the thermally stable data at 5 km, L' ranges from about -25 to about -5 m (the sign indicates the direction of forces). From figure 14, the boundary layer is clearly stopped at the base of the inversion (197 m). A rule of thumb is that the surface layer extends to a height equal to about one-tenth of the inversion height. In this case, the rule of thumb indicates that the surface layer should be about 20-m thick; this is in excellent agreement with the assumption that the height denoted by L' is also a good height at which to "cap" the surface layer. In stable situations, this argument breaks down; that is, the inversion is on the surface and there should be no "surface" layer; however, to maintain simplicity, the radiosonde gradient replaces the surface layer theory gradient at a height equal to the value of L' even for stable conditions.

The propagation loss, calculated by using the Jeske formulation with range dependent M profiles connected in range at a feature height and with the radiosonde M gradient replacing the surface layer model gradient for heights in excess of the calculated L' height, is shown in figure 15 as the open box symbol curve. There is little difference between the predictions with, or without, the replacement gradient at L'; the difference between the predicted and measured propagation loss is considerable.

A second modification to the surface layer theory forces the surface roughness parameter Z_0 to a value of 10^{-5} m. *Gossard & Strauch* [1983] indicate that this value is reasonable; although, most other researchers believe in somewhat higher and wind speed dependent values (see *Liu, Katsaros, & Businger*, [1979]). The solid upright triangle symbol curve, in figure 15, is the predicted propagation loss for the addition of this second modification to the procedures for creating the M profile from the Jeske formulation with range dependency feature connected and with the M gradient replacement at height L'. This technique follows the curves of the previous two M profile models and fails to match the measured data.

A third modification eliminates the range dependency and assumes that the surface meteorological measurements made at the F35 radar site are representative of the entire propagation path. The propagation loss for the Jeske formulation, feature height separation (11 points from the surface to the duct height and 10 points from above the duct height to 100 m), radiosonde M gradient replacement at L', Z_0 fixed to 10^{-5} m, and with no range dependency (i.e., the profile for the 0 km range is used for all ranges), is shown in figure 15 as the solid downward pointing triangle. Unlike the previous predictions, this curve is a better approximation to the measurements. For ranges beyond about 10 km, this prediction overestimates the detection range by about 2 km; however, for ranges beyond about 15 km, the assumption of a standard atmosphere is a better predictor. For ranges between about 2.5 to 12.5 km, the predictions, assuming that the surface measurements at F35 are representative of the path, are as good or better in representing the measured data than any other technique examined so far.

For this one case, analyzed by using the Jeske and variants of the Jeske surface layer model, the best agreement between predictions and observations occurs when the atmosphere is assumed to be range independent. This is not always the case, as will be shown in later sections. Before

proceeding to the next example, it is best to examine the techniques of the LKB model, which is the subject of the following section.

LKB Surface Layer Formulation and Its Variants

The LKB model is, in a sense, more pleasing than the Jeske formulation, because it does not require an empirical connection between L' and the physical observables. The added complexities of solving three equations for three unknowns are generally insignificant, except in highly stable conditions where the problem is ill-formed and the iterations fail; however, there are probably techniques for solving these ill-formed problems, but those topics are beyond the scope of this analysis. Suffice to say that only a few cases of actual surface measurements could not be handled by the LKB model.

Figure 17 complements figure 15, in that, it is the comparison of the propagation model using the LKB surface layer theory to the measured data. Like figure 15, the crosses denote the measured propagation loss between the radar and the target; the solid line is the predicted propagation loss, assuming propagation in a normal or standard atmosphere. The symbol curves are summarized as follows:

- Open circle symbol curve: The M profiles are developed from the full LKB theory (equations [9] through [13]) by using the range dependent surface meteorological data described in table 6. The M profiles are connected in range at a feature height (nominally the evaporation duct height under unstable conditions) where there are 11 pairs of height and M values between the surface and the feature height. There are 10 pairs of height and M values above the feature height extending to a height of 100 m.
- Open box symbol curve: Identical to the open circle symbol curve technique, except that the M gradient from the radiosonde replaces the M gradient from the surface layer theory at a height equal to the magnitude of the Monin-Obukhov length (equation [11]).
- Solid upward pointing triangle symbol curve: Same technique as for the open box symbol technique, except that Z_0 is set to a value of 10^{-5} m, effectively eliminating equations [12] and [13]).
- Solid downward pointing triangle symbol curve: This is the full LKB formulation, assuming that the surface meteorology measured at the F35 radar site is representative of the entire propagation path. In addition, the profile is created by using the logarithmic spacing of the "feature" type profile with the radiosonde M gradient replacing the LKB theory gradient at heights in excess of L', and the surface roughness parameter Z_0 is set to 10^{-5} m.

All four LKB techniques reasonably replicate the measured data, although there are certain ranges where each of the curves deviate from the measurements; however, comparing the error between the predicted and measured propagation loss, the figure gives the impression that the LKB techniques are superior to the assumption of a standard atmosphere.

For this one case, the LKB technique seems to be the best predictor; however, this is not always true for all of the cases examined, as will be seen in subsequent case studies.

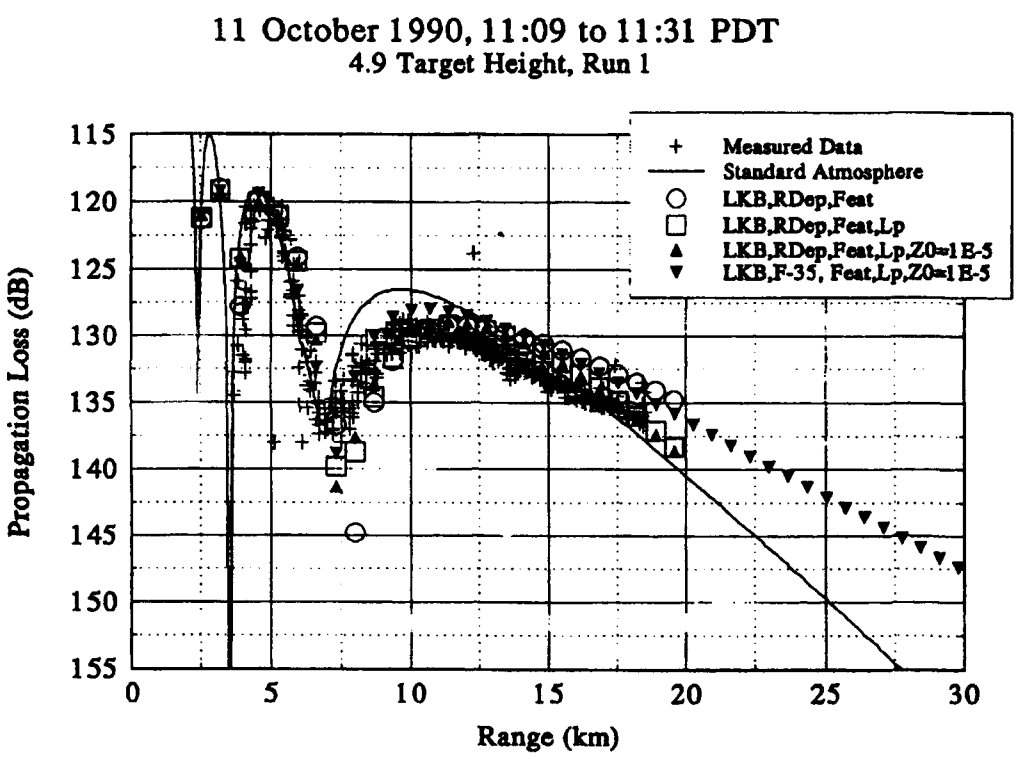

Figure 17. Comparisons of the measured (crosses) to the predicted propagation loss derived from the LKB (and variants) surface layer model for the run from 11:09 to 11:31 PDT made on 11 October 1990.

30 JANUARY 1991

The meteorological and radar measurements for this period are summarized in figures 18 through 22. An examination of the outbound run, from 12:23 to 12:54 PST, follows. The air and sea temperature traces (figure 18) show a generally warming trend with increasing range extending from the radar, and they indicate a range varying environment. Although the sea temperature recording experienced some problems (from about 09:15 to 10:35, and from 13:00 outward), the sensor and recording equipment were operating properly for the times of interest. The air and sea temperature traces are somewhat repeatable in range, which implies that the conditions are not time varying. At the radar site, the wind speed (figure 19) is increasing towards the afternoon, rising from near calm at 09:30 to about 8 kn at 13:00. Wind direction was nearly constant from the northwest. The relative humidity hovered around 60%; the air and sea temperatures gradually warmed. The air-sea temperature differences (figure 20) show thermally stable and unstable conditions along the path; whereas, at the radar site, the conditions were generally thermally unstable. The tidal variation (figure 21) shows that the tide was receding, and for the times of interest, the radar height is estimated to be constant at 23.8 m above the sea surface. (See Seq. No. 11 in table 4.) This is the median height of the radar above the water during the time period of 12:23 to 12:54 PST. The upper-air M profile (figure 22) shows a surface-based duct from an elevated layer (SBD condition), where the base of the inversion is at about 50 m. Table 7 lists the height and M-units for this sounding. Figure 23 plots the predicted propagation

loss in a height-range space for the radar with the M profile of figure 22. There is little difference, for a target at 4.9 m, between the propagation loss for standard atmospheric conditions (figure 9) and the propagation loss in this SBD environment, out to ranges of about 20 km. In this case, the SBD affects propagation (for the 4.9-m target) at ranges beyond 20 km. Because the run was terminated at about 16 km, the SBD should have little effect on propagation, and the controlling propagation mechanisms should be confined to a layer extending from the surface to an altitude of about 50 m, for example, the boundary layer. Table 8 lists the analyst interpretation of the observed surface data.

Jeske Surface Layer Formulation and Its Variants

The data from table 8 are used to compute the modified refractivity profiles, in the same way as was done for the 11 October 1990 case examined earlier. Figure 24 shows the comparisons of the measured propagation loss to the results of propagation calculations using the Jeske and variants of the Jeske method. The crosses on this plot show the measured propagation loss between the radar and the target—the isolated crosses (between ranges of 5 and 16 km and between 124- and 130-dB loss) are probably due to misfires of the radar transponder. It is likely that the transponder fired with 0-μs delay (simulating return from the target), and it is difficult to separate transponder and target returns. These "extraneous" returns were left in the subsequent analyses, but were smoothed out by taking the medians of the measured "return." Clearly, the largest grouping of returns in a small range bin are due to the target and not the transponder. The solid line (figure 24) is the prediction of propagation loss in a standard atmosphere. The open circle symbol trace corresponds to a M profile created using the Jeske formulation with range varying surface meteorological conditions (listed in table 8), and feature connected (at the duct height) in range. The open square symbol curve corresponds to modifying the aforementioned profile with the radiosonde gradient, 0.1025 M/m, at the height defined by $|L'|$. (Refer to table 7.)

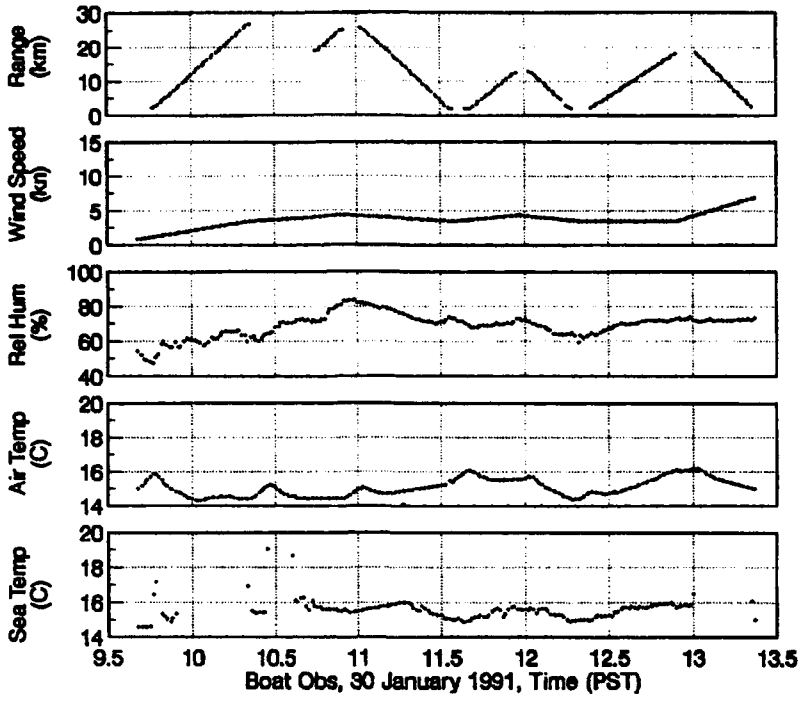

Figure 18. Surface meteorological observations recorded by the sensors on the boat, with the ranges from the boat to the radar, for the measurements on 30 January 1991.

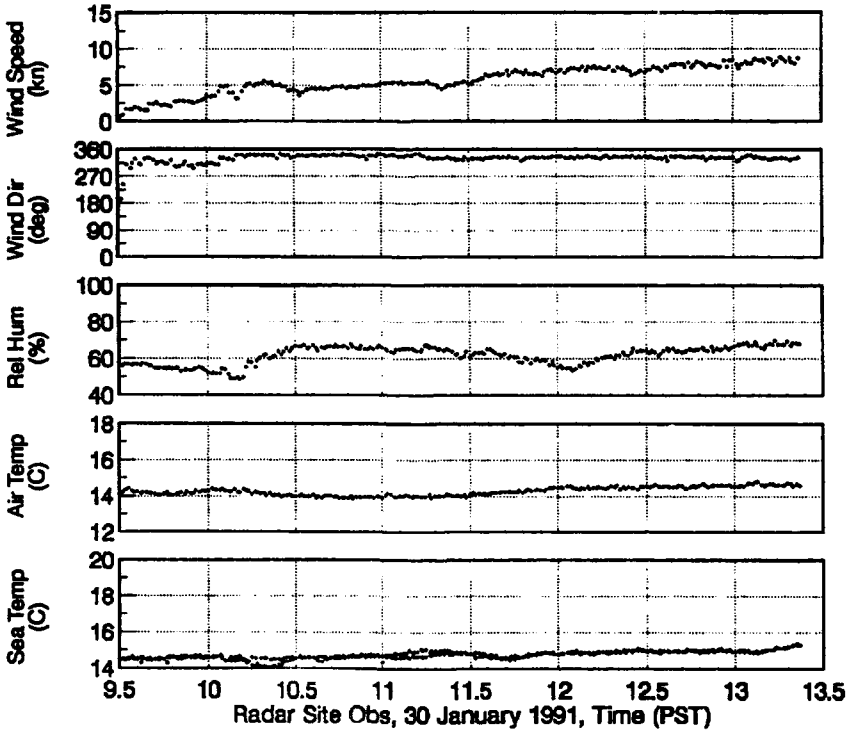

Figure 19. Surface meteorological observations recorded by the sensors on land near the radar F35 site for the measurements on 30 January 1991.

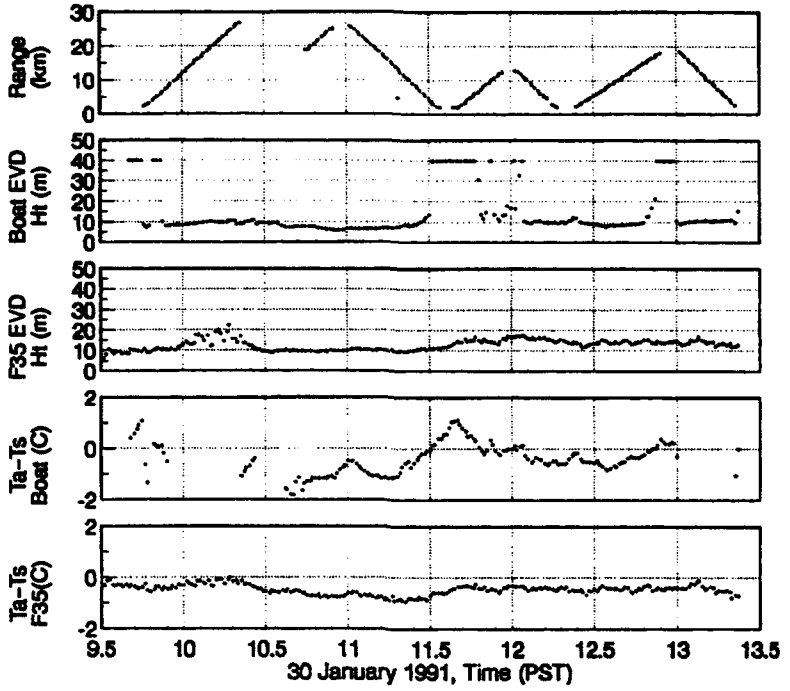

Figure 20. Range from the radar to the boat, evaporation duct heights (Jeske formulation) calculated from surface observations made on the boat and near the radar, and air-sea temperature difference observations made on the boat and near the radar site for 30 January 1991.

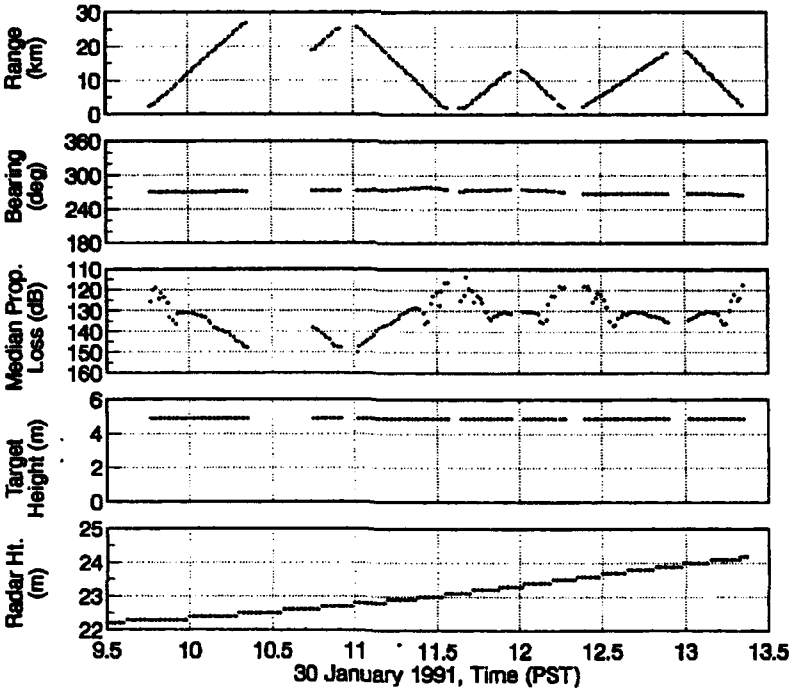

Figure 21. Range from the radar to the boat, azimuth bearing of the boat from the radar, median propagation loss between the radar and the boat, target height on the boat, and the height of the radar above the water for the measurements on 30 January 1991.

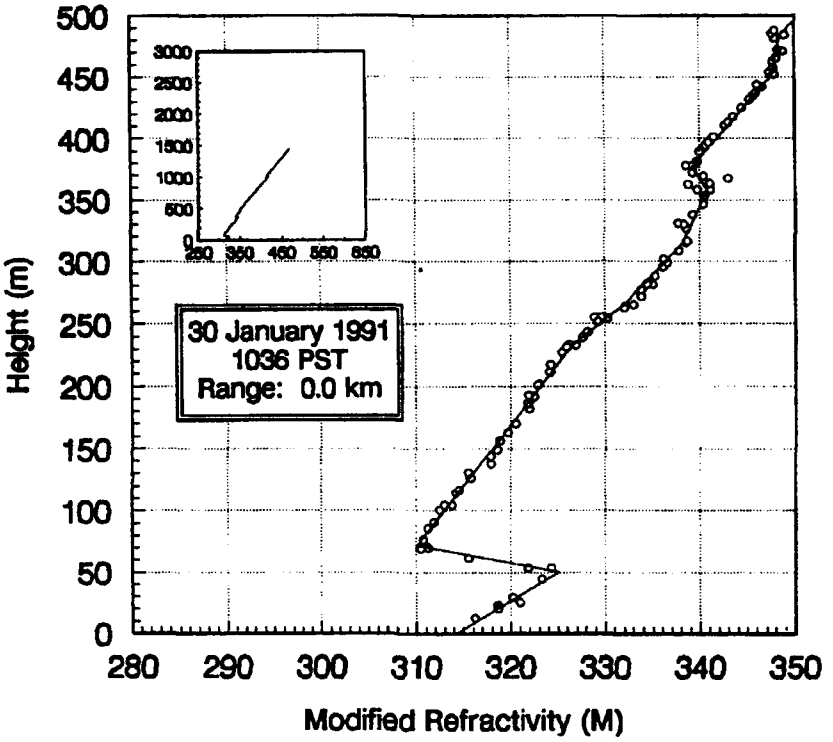

Figure 22. The M profile as measured by the radiosonde launched from the boat, 2 km away from the radar site, on 30 January 1991 at 12:02 PST.

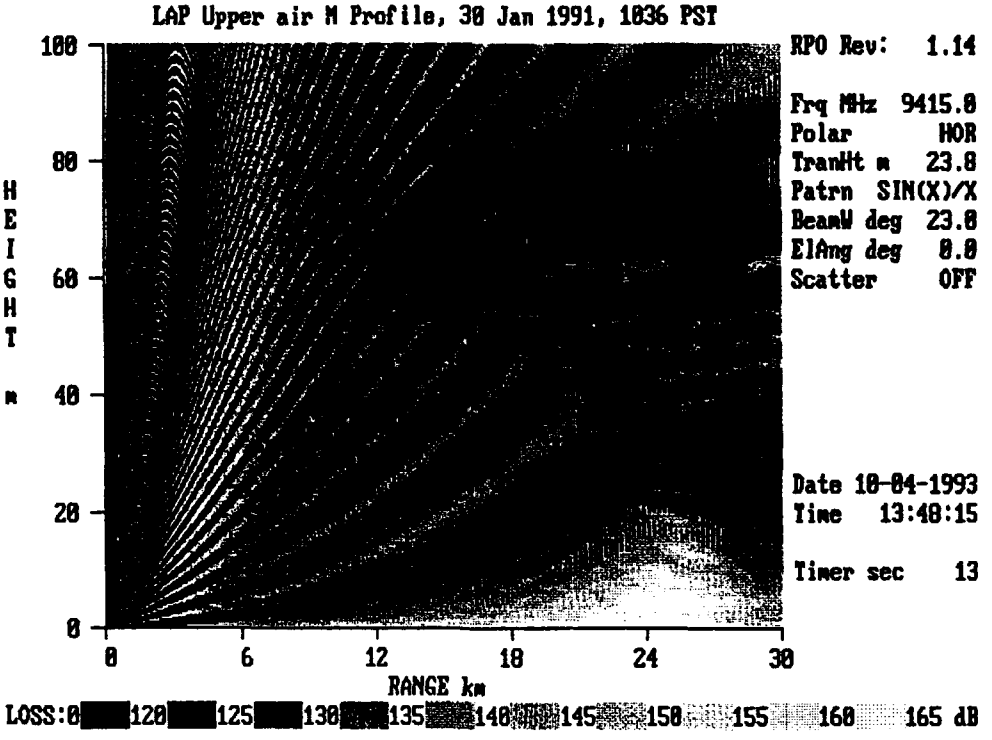

Figure 23. Predicted propagation loss in a height range space for the M profile shown in figure 22. The effects of the surface-based duct are not observed until the target is at a range of about 20 km.

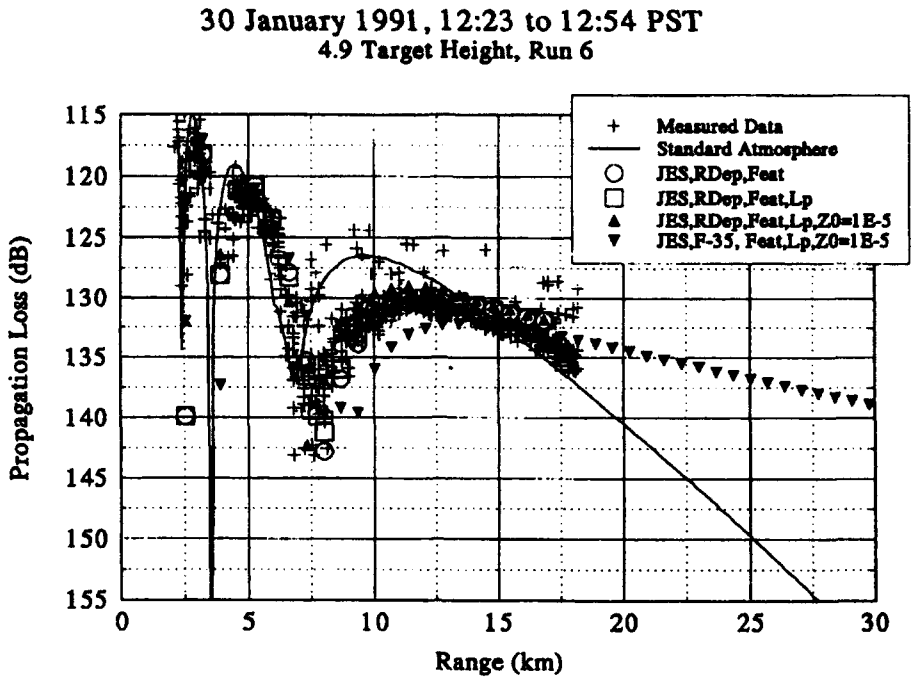

Figure 24. Comparisons of the measured (crosses) to the predicted propagation loss derived from the Jeske (and variants) surface layer model for the run from 12:23 to 12:54 PST made on 30 January 1991.

The solid upward pointing triangle curve is the same as the open square symbol curve, but Z_0 is set to 10^{-5} m. The downward pointing solid triangle symbol curve corresponds to a range independent—assume that the measurements at the radar site are applicable to the entire path—feature connected radiosonde gradient replacement at height $|L'|$, and Z_0 set to 10^{-5} m. The standard profile prediction (solid line) underestimates the propagation loss for ranges from about 4 to 12.5 km. Propagation loss predictions using the range varying Jeske and variant profiles reasonably match the measured propagation loss over all ranges. The range independent prediction (solid downward pointing triangle) tends to overestimate the propagation loss for ranges between 7 and 13 km.

Compared to the standard atmosphere prediction curve, two important points are readily observed in figure 24: the shift in range of the last interference null (from about 6.5 km to about 7.5 km), and the depression in signal amplitude at the last interference peak.

Figure 25 illustrates the shape of the M profiles calculated by using the unaltered Jeske formulation of the surface layer. The range dependent values of L', shown in the lower left hand section of figure 25, vary from -108.6 (at 15 km) to +83.6 (at 17.5 km). L' is about -10 for ranges between 5 and 10 km. The rule of thumb, that the surface layer is about 10% of the inversion height (50 m), indicates that the surface layer should extend to about 5 m. (See figure 22 and table 7.) The values of L' are at least twice as large as the rule of thumb would predict; however, the comparisons of the predicted propagation loss to the measured propagation loss are fairly good for the range varying environmental conditions with the radiosonde gradient replacement at the height of $|L'|$.

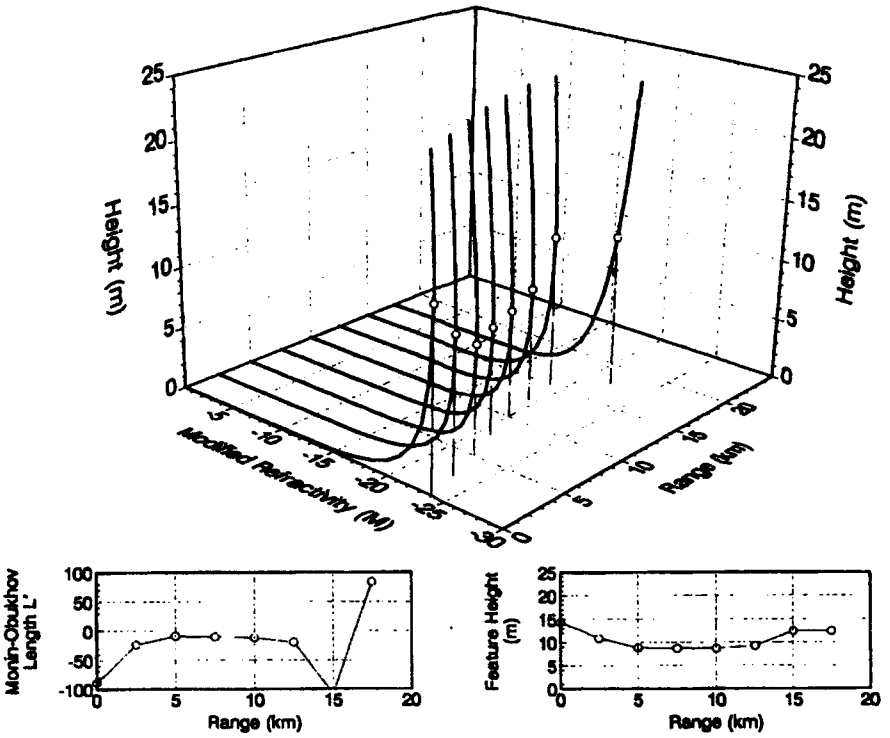

Figure 25. Range dependent height and modified refractivity profiles derived from the Jeske model for the surface meteorological data listed in table 8.

LKB Surface Layer Formulation and Its Variants

Figure 26 complements figure 24, in that, it is the comparison of the propagation model (using the LKB surface layer theory) to the measured data. Like figure 24, the crosses denote the measured propagation loss between the radar and the target—the solid line is the predicted propagation loss assuming propagation in a normal or standard atmosphere. The symbol curves are summarized as follows:

- Open circle symbol curve: The M profiles are developed from the full LKB theory (equations [9] through [13]) using the range dependent surface meteorological data described in table 8. The M profiles are connected in range at a feature height (nominally the evaporation duct height under unstable conditions), where there are 11 pairs of height and M values between the surface and the feature height. There are 10 pairs of height and M values above the feature height extending to a height of 100 m.
- Open box symbol curve: Identical to the open circle symbol curve technique, except that the M gradient from the radiosonde replaces the M gradient from the surface layer theory at a height equal to the magnitude of the Monin-Obukhov length (equation [11]).
- Solid upward pointing triangle symbol curve: Same technique as for the open box symbol technique, except that Z_0 is set to a value of 10^{-5} m, effectively eliminating equations [12] and [13].
- Solid downward pointing triangle symbol curve: This is the full LKB formulation, assuming that the surface meteorology measured at the F35 site is representative of

the entire propagation path. In addition, the profile is created by using the logarithmic spacing of the "feature" type profile with the radiosonde M gradient replacing the LKB theory gradient at heights in excess of L', and the surface roughness parameter Z_0 set to 10^{-5} m.

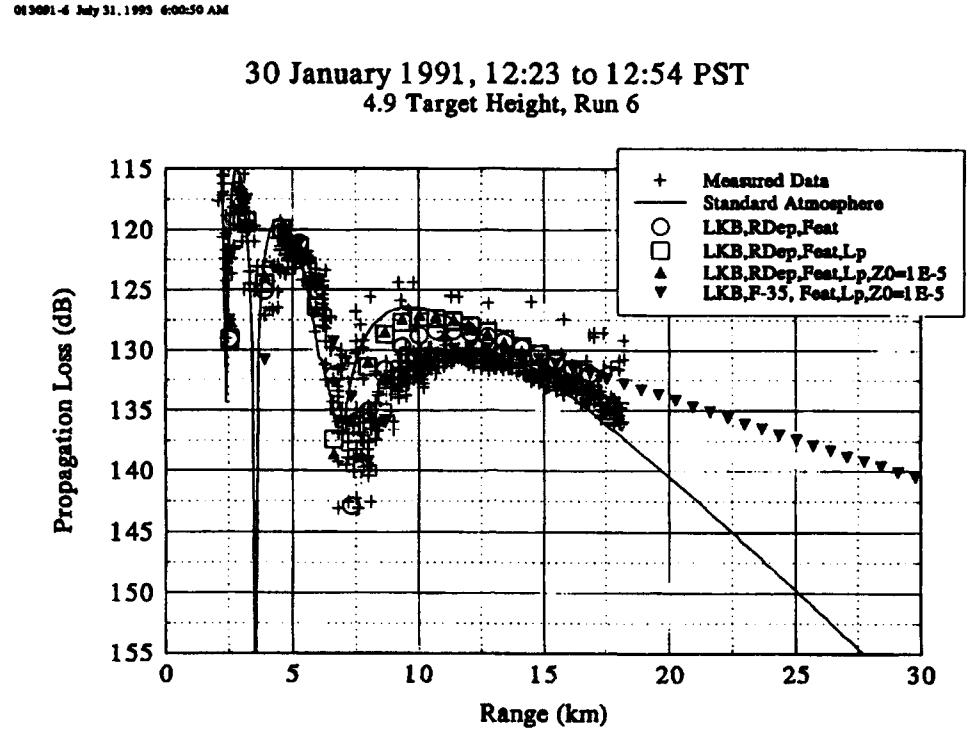

Figure 26. Comparisons of the measured (crosses) to the predicted propagation loss derived from the LKB (and variants) surface layer model for the run from 11:23 to 12:54 PST made on 30 January 1991.

For ranges to about 13 km, the propagation loss predicted by using the range independent, feature connected, radiosonde gradient replacement at $|L'|$, with Z_0 set to 10^{-5} m, appears to be the best match to the measured propagation loss. Between the ranges of 8 to 15 km the predictions derived from the unaltered LKB formulation underestimate the propagation loss by a few dB.

For this case, the Jeske technique, including range dependency, seems to be the best predictor.

5 DECEMBER 1991

The meteorological and radar measurements for this day are summarized in figures 27 through 31, and table 9. A detailed look at the first outbound run, from 12:06 to 12:29 PST, follows. In figure 27, the range traces (top plot) show data only between 12:06 to 12:29 PST and between 13:54 and 14:17 PST. In between these times (12:29 to 13:54 PST), the recording circuits of the radar failed and no radar data were archived. During the times of interest (12:06 to

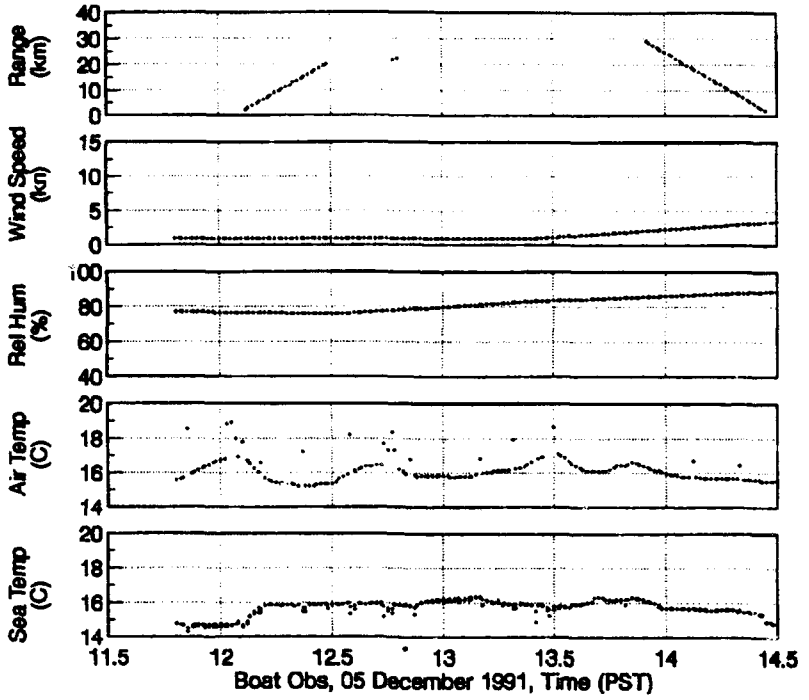

Figure 27. Surface meteorological observations recorded by the sensors on the boat and the range from the boat to the radar for the measurements on 5 December 1991.

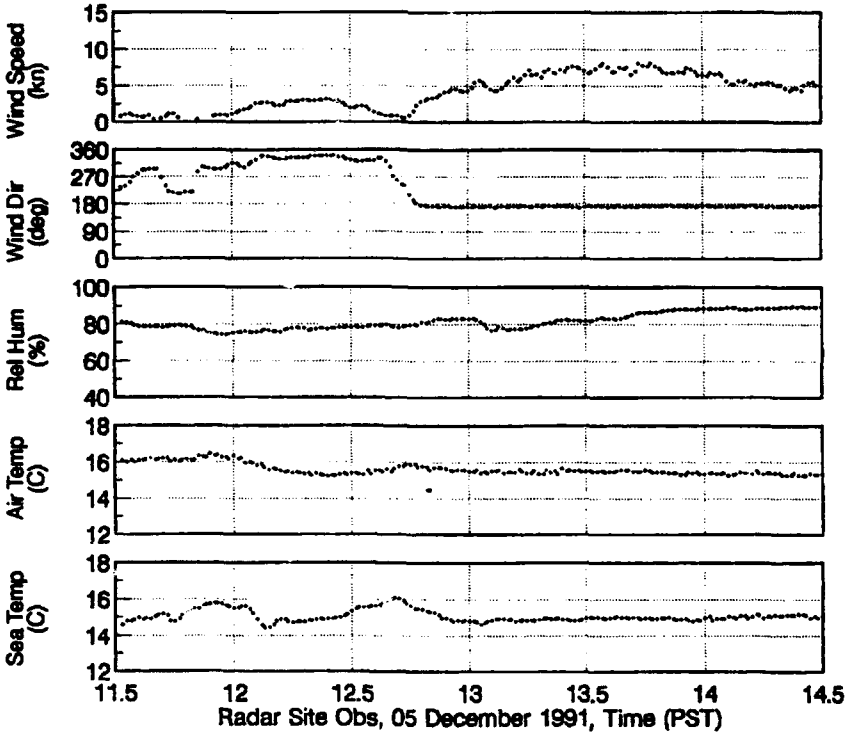

Figure 28. Surface meteorological observations recorded by the sensors on land near the F35 radar site for the measurements on 5 December 1991.

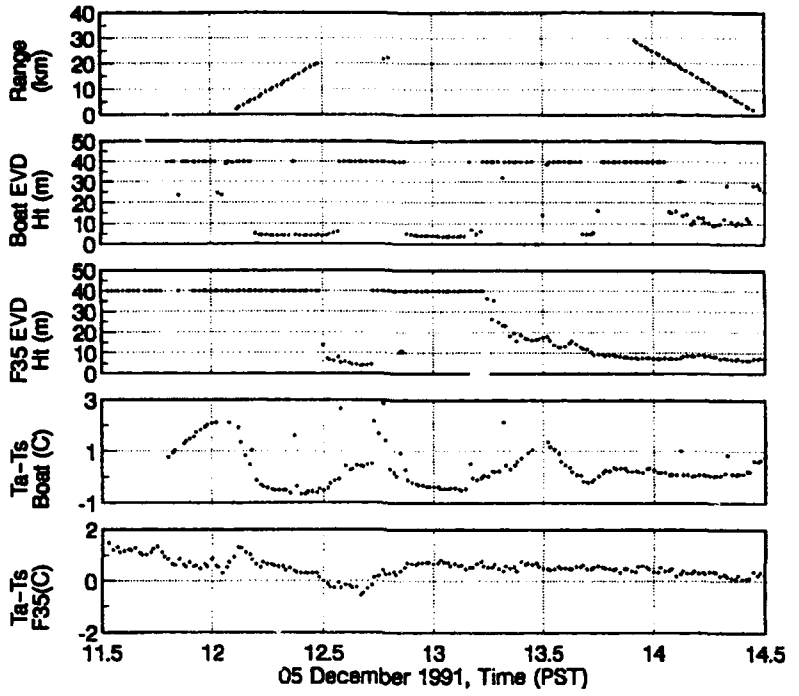

Figure 29. Range from the radar to the boat, evaporation duct heights (Jeske formulation) calculated from surface observations made on the boat and near the radar, and air-sea temperature difference observations made on the boat and near the radar site for 5 December 1991.

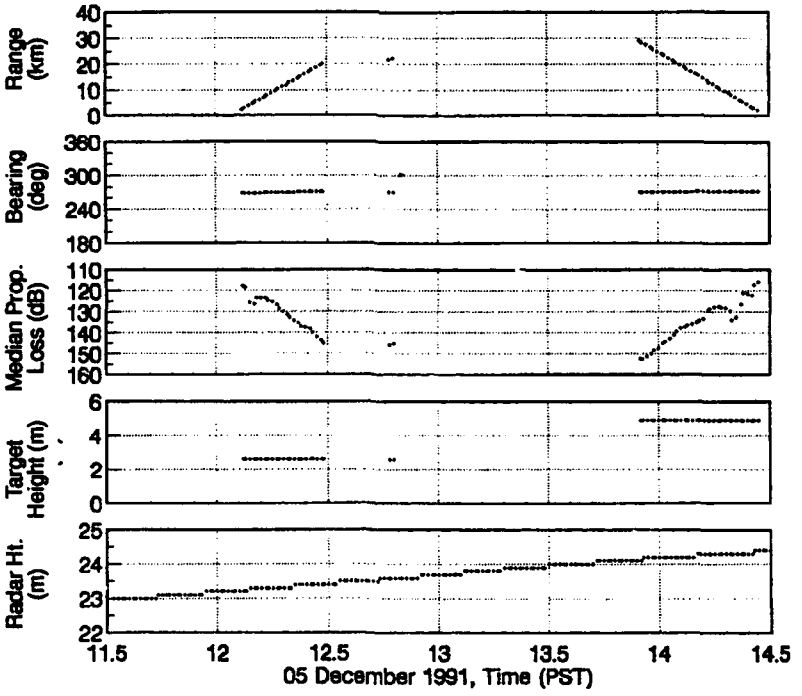

Figure 30. Range from the radar to the boat, azimuth bearing of the boat from the radar, median propagation loss between the radar and the boat, target height on the boat, and the height of the radar above the water for the measurements on 5 December 1991.

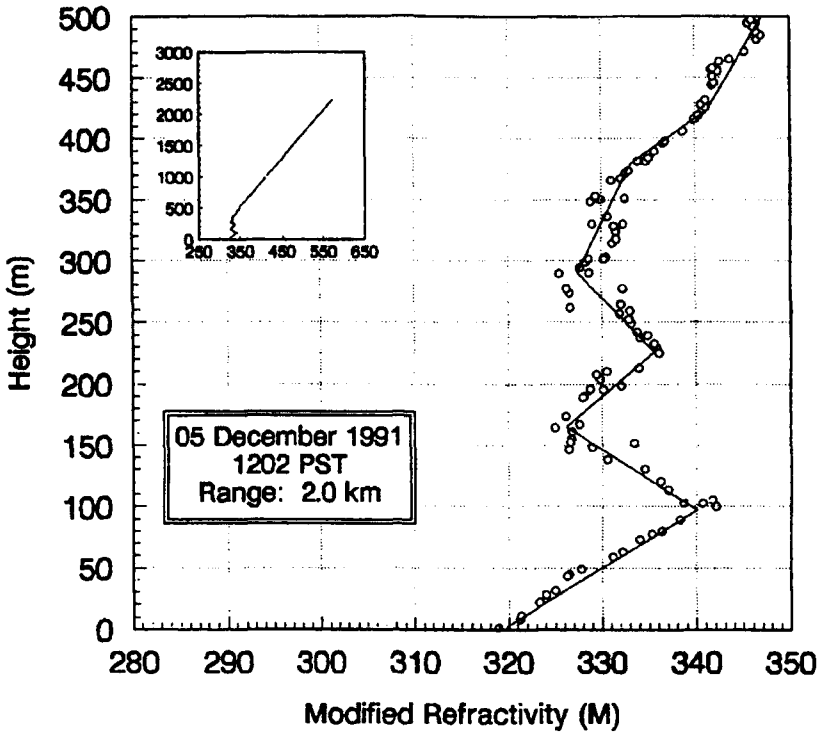

Figure 31. The M profile as measured by the radiosonde launched from the boat, 2 km away from the radar site, on 5 December 1991 at 12:02 PST.

12:29 PST), the wind speed, about 1 km, measured on the boat (figure 27) was low; whereas, the wind speed measured at the radar (figure 28) was somewhat higher at about 2.5 kn. The air temperature, measured on the boat, indicated both a temporal and range varying condition. In the outbound run, the air temperature was warmer near the radar and decreased with greater range. In the inbound run (13:54 to 14:17 PST), the air temperature was warmest at the farthest range (30 km), and it decreased as the boat came back towards to the radar.

The environmental time dependency is best illustrated as looking at the plot of wind direction as measured at the F35 site (figure 28). The wind is from the southwest at the start of the measurements (11:30 PST); wind direction changes to northwest; it changes to southwest, and from about 11:50 PST onward, the wind direction is from the north northwest. At about 12:40 PST, the wind direction changes to almost due south. The range dependent thermal stability (figure 29) is volatile. At the start of the outbound run, the air-sea temperature difference close to the radar is about +2 degrees C. At the furthest range of the outbound run (20 km), the air-sea temperature difference is about –0.5 degree C. In the same period of time, the stability at the radar site is always positive, from about +1 to +0.5 degree C. As was mentioned earlier, from 01 August 1991 and on, the aft facing corner reflector was lowered to a height of 2.6 m above the water, and the target height for the times of interest is now 2.6 m. For the times between 12:06 and 12:29 PST, the tide was nearly normal (figure 30), and the median radar height above the water is 23.3 m. (See table 4.) Table 9 lists the analyst interpretation of the observed surface meteorological data.

Figure 31 is the upper-air M profile, approximately 2 km from the radar, measured from the boat at 12:02 PST. The height and M-units for this profile are listed in table 10. There are two

elevated trapping layers: the first between 97 m and 165 m in altitude; and the second between 226 and 290 m in altitude. The base of the first inversion (97 m) implies, through the rule of thumb, that the surface layer should extend to an altitude of about 10 m.

Figure 32 is the upper air M profile measured from the boat, approximately 20 km from the radar, at 12:45 PST, and the data are listed in table 11. This profile is substantially different from the profile that was measured 43 minutes earlier and 18 km closer in range. The lowest M gradient in height (from 0 to 50.18 m) is probably incorrect, as the surface value of temperature and humidity were derived from a different set of sensors (observations from a psychrometer on board the boat) than the data above 50.18 m. The radiosonde receiver located at the radar site was not able to detect the radiosonde signal until the sonde was at an altitude of about 50 m. More than likely, the M gradient in the next highest layer (50.18 to 168.46 m) should be extrapolated to the surface. The base of the inversion is at about 168 m and the rule of thumb is that the surface layer should extend from the surface to about 17 m.

Jeske and LKB Surface Layer Formulations and Their Variants

Figures 33 and 34 show the comparison of the measured propagation loss to the results of propagation calculations using the Jeske and LKB surface layer models (and their variants). In both cases, the unaltered, range dependent, feature connected model (open circle symbols) results are significantly different from the measured propagation loss. The comparison of measured to standard atmosphere results are very good. The Jeske variants overestimate the propagation loss near the last optical peak; whereas, the LKB variants, especially the range dependent, feature connected, $|L'|$ limited, results are in good agreement with the measurements (they also closely follow the standard atmosphere results).

For meteorological conditions that indicate the environment is range and time dependent, it is surprising to see that the predictions derived from the assumption of a standard atmosphere agree with the measurements. In fact, the results from the assumption of a standard atmosphere appear to fit the measurements as the best of all models.

Three cases have been examined: in the first case, the results from the LKB model are the best fit to the measured data; in the second case, the results from the Jeske model are the best fit to the measured data; and in the final case, the results from the assumption of a standard atmosphere are the best fit to the measured data. The question of which one of the models is best overall is addressed in the subsequent sections.

STATISTICS

Tables 12 and 13 present the measured detection range at four propagation loss thresholds for all applicable inbound and outbound runs. Table 12 lists the measured detection ranges for the 4.9-m target height; table 13 lists the ranges for the 2.6-m target height. The first column, labeled **Seq. No.** corresponds to the first column of table 4. The second column, labeled **Filename MoDaYr.Run** is the name of the archived radar data file, where the filename extension is a two-digit identifier. Even-numbered filename extensions indicate outbound runs, and odd-numbered filename extensions indicate inbound runs. The last four columns are the detection ranges for the specified propagation loss thresholds. These detection ranges were derived from the raw data (including transponder hits) by taking the median value of the observed propagation loss in a 200-m wide range bin and then comparing this value to each of the four thresholds

(125, 130, 135, and 140 dB). The furthest range, where the median observed propagation loss was less than the threshold, is declared the radar detection range.

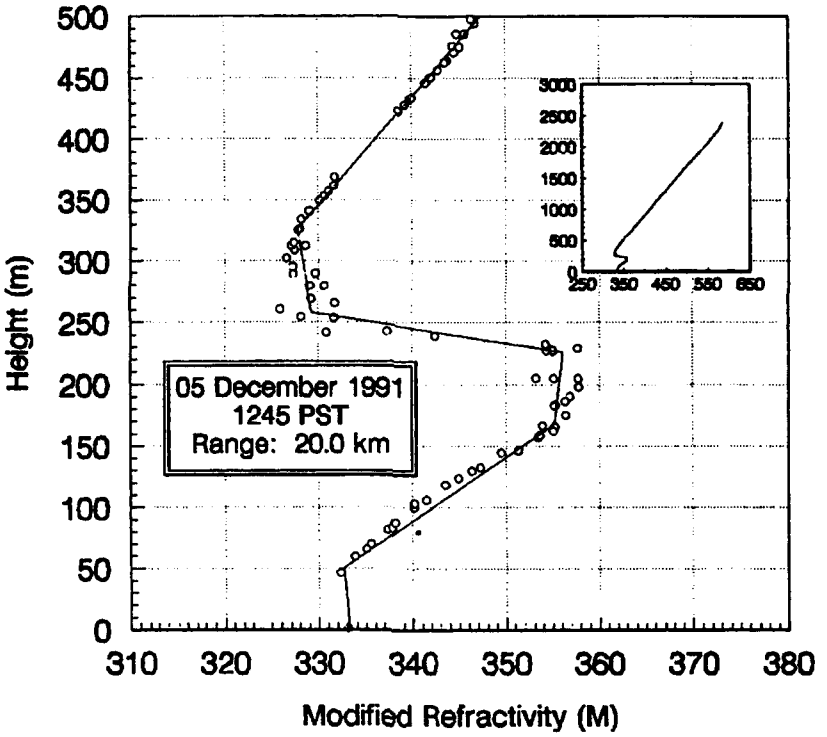

Figure 32. The M profile as measured by the radiosonde launched from the boat, 20 km away from the radar site, on 5 December 1991 at 12:45 PST.

120591-0 July 30, 1993 6:31:14 PM

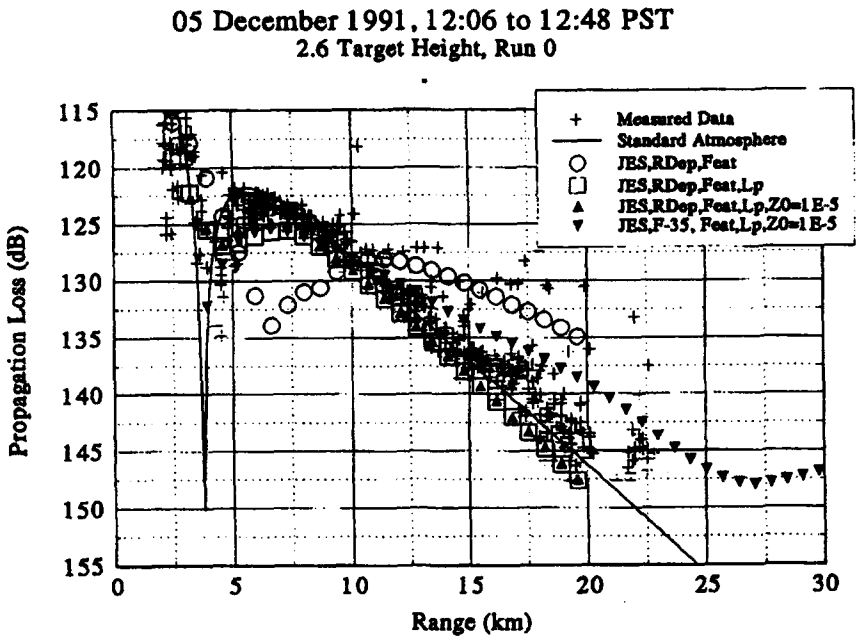

Figure 33. Comparisons of the measured (crosses) to the predicted propagation loss derived from the Jeske (and variants) surface layer model for the run from 12:06 to 12:48 PST made on 5 December 1991.

120591-0 July 31, 1993 7:34:34 AM

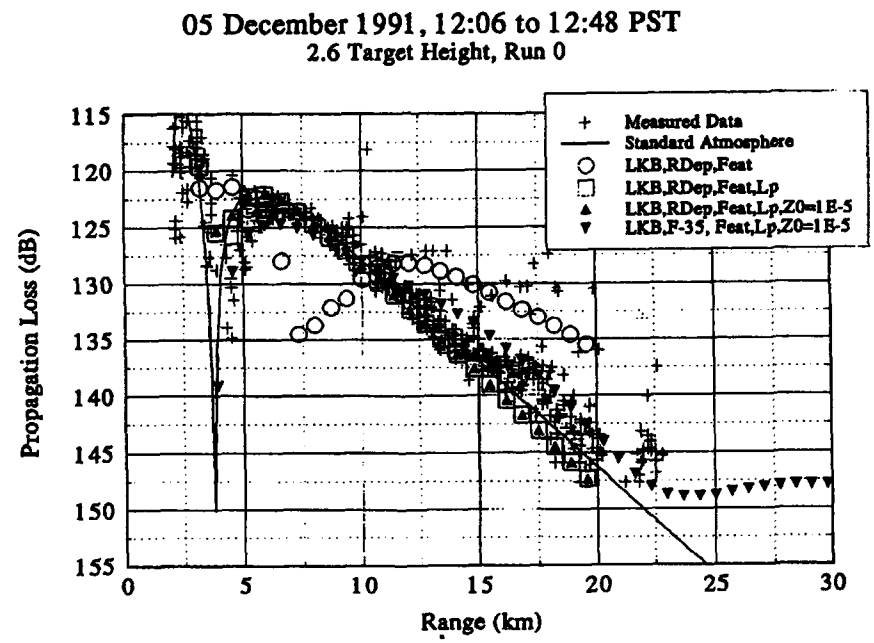

Figure 34. Comparisons of the measured (crosses) to the predicted propagation loss derived from the LKB (and variants) surface layer model for the run from 12:06 to 12:48 PST made on 5 December 1991.

For example, the radar data for the second run on 10 October 1990 (Seq. No. 2, filename 101190.01) is shown in figure 15. On this figure, there is one isolated radar hit at about 124 dB at a range of about 12 km. Without a filter, this would be declared the maximum detection range for the 125-dB threshold, and, more than likely, this would be wrong. With the median filter described above, the furthest range where the measured propagation loss is greater than 125 dB occurs at a range of 5.70 km, which is the entry in column 3 of table 12 for this data file. An "eyeball" estimation of the detection ranges for the first three thresholds agrees with the data listed in table 12; however, in figure 15, the measured propagation loss *never* exceeds 140 dB. The boat stopped short of the range where the loss would exceed 140 dB, and the entry "NaN" (Not a Number) is used to indicate such a situation (e.g., the entry in column 6 of table 12 for this run).

Table 14 is a cross reference, keyed by a letter designator, to the surface layer models (Jeske & LKB) and the variants of these models used in the following analysis. The letter designators B, D, F, and H correspond to the LKB model and its variants that are feature connected refractive profiles (comparisons of results from these models to measured data are shown in figures 17, 26, and 34). Likewise, the letter designators N, P, R, and T correspond to the Jeske model and its variants that are feature connected refractive profiles (comparisons of results from these models to measured data are shown in figures 15, 24, and 33). Eight additional variants of the surface layer models are used to create refractive profiles. These variants are similar to the models discussed above, but do not use the feature connected method of vertical height spacing; instead, these variants use 100 samples in the vertical with a fixed height spacing of 87.5 cm between samples.

Tables 15 and 16 list the average, median, and variance of the difference between the measured and the predicted radar detection range for propagation loss thresholds of 125, 130, 135, and 140 dB. The target height is 4.9 m. For a threshold of 125 dB, the average difference between radar detection range predictions using a standard atmosphere (refractivity profile designator of "Std") and the measured radar detection ranges is –0.10 km (the negative sign indicates that the measured detection range is less than the predicted). The median error is 0.0 km and the variance of the error is 0.20 km. (See table 15.) Detection range predictions made by assuming a standard atmosphere are the "best" comparisons to the observed detection ranges, in the sense that the results yield the minimum average, median, and variance errors. The model with the next best performance is the model described by the letter designator "H" (LKB, non-range dependent, feature connected, L' limited with a fixed Z_0). For a threshold of 130 dB, the assumption of a standard atmosphere is not bad (average, median, and variance of errors are –1.60, –1.20, and 4.70 km, respectively), but the results from the model described by designator "G" (LKB non-range dependent, fixed height spacing, L' limited with fixed Z_0) are slightly better. In terms of minimizing the median error, models "A" and "B" (LKB) are best (both models result in a 0.00-km median error in detection range).

Table 17 and 18 are the results from comparing the predicted to the observed detection ranges for the 2.6-m target. For a 125-dB threshold, models "B," "D," "E," "F," and "R" all perfectly match the observation in the median sense. Of these five models, "F" (LKB, range dependent, feature connected, L' limited with fixed Z_0) has the lowest variance (3.00 km).

Table 19 presents the variance of the average error, median error, and variance of the error for all four propagation loss thresholds and for each of the two target heights. The unaltered, fixed-height-spacing Jeske model (designator "M") produces results that are the worst compared

to the observed. The variance of the variance-of-error for the 4.9-m target height is 2076.98 km and the variance of the median error is 21.20 km! The assumption of a standard atmosphere produces results that minimize the variance of the variance, but model "C" (LKB, range dependent, incremental, L' limited with fixed Z_0) minimizes the variance of the median error.

Table 20 sorts the listing from tables 15 and 16 (4.9-m target height) in terms of the median difference between the predicted and the measured detection range. The column labeled composite threshold lists the sorted results considering all four propagation loss thresholds. Table 21 sorts the same listings in terms of the variance of the differences. It is surprising to see how strong the assumption of a standard atmosphere is. From table 21, the assumption of a standard atmosphere is shown to minimize the variance of the error in three of the four propagation loss categories, and it minimizes the variance of the error considering all four thresholds. In four out of five categories, the assumption of a standard atmosphere minimizes the variance of the difference between the predicted and observed detection range.

Tables 22 and 23 summarize the sorted median difference and variance of difference, for the 2.6-m target height, respectively. For the lower target height, the assumption of a standard atmosphere appears to be even better than it is for the 4.9-m target, taking two of five categories in the median sense (table 22) and taking four of five categories in the variance sense (table 23).

CONCLUSIONS

The evaporation duct significantly affects X-band radar detection capabilities of low-altitude targets at all ranges. Within the horizon, the duct may shift the location of the last interference null several kilometers in range, which may cause nondetection at ranges where detection is expected and detection at ranges where detection is not expected. In addition, the evaporation duct may reduce the signal strength at ranges near the last interference peak, such that detection of low-altitude targets may not be possible until the target is much closer. These effects have been observed in a carefully controlled radar experiment.

At ranges beyond the last optical peak, the radar signal strength depends both on the surface layer and on the mixed layer. To accurately model propagation in this region, knowledge of both surface layer and upper-air meteorology is required. Empirical models to merge the surface layer with the mixed layer have been developed; however, additional studies and measurements are needed to refine these models.

The assumption of a standard atmosphere tends to minimize the variance of the difference between predicted and observed radar detection range; however, the LKB surface layer model (extending from the surface to a height of the magnitude of the Monin-Obukhov length) seems to minimize the median of the difference between predicted and observed detection range. Detection ranges that are predicted by using a standard atmosphere are generally "close" to the observed detection ranges, which tend to keep the variance of the error small. Detection ranges that are predicted by using a variant of a surface layer model (e.g., the LKB terminated at $|L'|$) are, in the median sense, better than predictions derived from the assumption of a standard atmosphere, but a few cases are considerably different from observations. This trend keeps the median error small but the variance of the error large.

Remote sensing of the environment by use of an X-band radar, in conjunction with modern numerical modeling capabilities, has proven to be a valuable tool in the understanding and utilization of tropospheric propagation.

Table 1. Furuno Model 2050X radar parameters.

Parameter	Capabilities
Frequency	9,415.0 MHz
Peak Power	50.0 kW
Pulse Width	0.8 μs
Pulse Repetition Rate	600.0 Hz
Noise Figure	6.0 dB
System Loss (estimated)	3.5 dB
Antenna	2.0 m Slot
Antenna Height	23.5 m msl
Polarization	Horizontal
Vertical Beamwidth	23.0 deg
Horizontal Beamwidth	1.2 deg
Antenna Gain	29.0 dBi
Rotation Rate	26.0 rpm

Table 2. Vega Model 363X transponder characteristics.

Parameter	Capabilities
Frequency	9,415.0 MHz
Peak Power	700.0 kW
Pulse Width	0.4 μs
Framing Pulse 1 Delay	6.0 μs
Framing Pulse 2 Delay	36.0 μs
Antenna	Slot
Antenna Height (on boat)	4.5 m
Vertical Beamwidth	15.0 deg
Horizontal Beamwidth	360.0 deg
Antenna Gain	7.5 dBi

Table 3. Meteorological sensor characteristics.

Sensor	Manufacturer	Model	Accuracy
Air Temperature	Rotronics	MP100F	0.2 deg C
Relative Humidity	Rotronics	MP100F	1.0%
Wind Speed	WeatherMeasure	2030	1.0%
Wind Direction	WeatherMeasure	2020	1.0 deg
Sea Temperature	Everest Interscience	4000	0.5 deg C
Sea Temperature	Ryan Instruments	RTM-1	0.3 deg C

Table 4. Summary information for the 54 measurement sets.

Seq. No.	Date	Start Time	End Time	Raob Launch Time	Local Time Zone	Radar Height (m)	Target Height (m)	Refractive Condition
1	10/11/90	10:41	11:03	11:54	PDT	23.40	4.90	SBD
2	10/11/90	11:09	11:31	11:54	PDT	23.40	4.90	SBD
3	11/20/90	11:23	12:20	10:57	PST	22.90	4.90	NOR
4	11/20/90	12:31	13:13	10:57	PST	23.20	4.90	NOR
—	12/06/90	10:03	10:39	10:49	PST	22.70	4.90	STL
—	12/06/90	10:51	11:28	10:49	PST	22.60	4.90	STL
—	12/06/90	11:36	12:09	10:49	PST	22.60	4.90	STL
—	12/06/90	12:17	12:38	10:49	PST	22.60	4.90	STL
5	12/11/90	09:47	11:02	10:41	PST	23.90	4.90	ELV
6	12/11/90	11:54	12:31	11:17	PST	24.20	4.90	STL
7	12/18/90	09:58	10:39	10:32	PST	22.60	4.90	NOR
8	12/18/90	10:55	11:26	11:17	PST	22.80	4.90	NOR
—	01/16/91	10:27	11:18	11:49	PST	22.80	4.90	SBD
—	01/16/91	11:24	12:10	11:49	PST	23.20	4.90	SBD
9	01/30/91	09:46	10:20	10:36	PST	22.40	4.90	SBD
10	01/30/91	11:01	11:33	10:36	PST	22.90	4.90	SBD
—	01/30/91	11:39	11:56	10:36	PST	23.20	4.90	SBD
—	01/30/91	12:01	12:16	10:36	PST	23.40	4.90	SBD
11	01/30/91	12:23	12:54	10:36	PST	23.80	4.90	SBD
12	01/30/91	13:01	13:21	10:36	PST	24.10	4.90	SBD
13	02/13/91	10:06	10:42	09:56	PST	23.00	4.90	SBD
14	02/13/91	10:49	11:19	09:56	PST	23.30	4.90	SBD
15	03/06/91	10:17	11:36	10:06	PST	23.80	4.90	STL?
16	03/06/91	11:44	12:21	10:06	PST	23/60	4.90	STL?
17	03/11/91	13:12	14:30	13:03	PST	24.40	4.90	NOR
18	03/11/91	14:37	15:11	13:03	PST	24.20	4.90	NOR
19	03/14/91	10:15	11:33	10:06	PST	23.50	4.90	NOR
20	03/14/91	12:04	12:35	11:56	PST	24.10	4.90	NOR

(Contd)

Table 4. Continued.

Seq. No.	Date	Start Time	End Time	Raob Launch Time	Local Time Zone	Radar Height (m)	Target Height (m)	Refractive Condition
21	04/30/91	10:00	10:42	09:50	PDT	23.40	4.90	ELV
22	04/30/91	10:48	11:16	09:50	PDT	23.30	4.90	ELV
—	04/30/91	11:26	11:41	12:10	PDT	23.30	4.90	ELV
—	04/30/91	11:47	11:58	12:10	PDT	23.30	4.90	ELV
23	08/01/91	13:13	14:01	13:06	PDT	22.80	2.60	ELV
24	08/01/91	14:08	14:36	13:06	PDT	22.80	4.90	ELV
—	08/01/91	14:44	15:04	13:06	PDT	22.90	2.60	ELV
—	08/01/91	15:12	15:27	13:06	PDT	23.00	4.90	ELV
25	08/08/91	12:02	12:39	11:59	PDT	23.50	2.60	ELV
26	08/08/91	12:48	13:17	11:59	PDT	23.70	4.90	ELV
27	08/15/91	12:06	12:46	11:59	PDT	22.80	2.60	NOR
28	08/15/91	12:54	13:27	11:59	PDT	22.70	4.90	NOR
29	09/12/91	11:44	12:21	11:53	PDT	22.60	2.60	ELV
30	09/12/91	12:30	12:54	13:12	PDT	22.60	4.90	ELV
31	10/10/91	12:04	13:01	11:54	PDT	22.70	2.60	STL
32	10/10/91	13:09	13:44	11:54	PDT	23.00	4.90	STL
33	10/24/91	13:05	14:11	13:01	PDT	23.60	2.60	NOR
34	10/24/91	14:17	14:49	13:41	PDT	24.10	4.90	NOR
35	12/05/91	12:06	12:48	12:02	PST	23.30	2.60	ELV
36	12/05/91	13:54	14:27	14:39	PST	24.30	4.90	SBD
37	12/12/91	10:37	11:05	10:35	PST	23.20	2.60	ELV
38	12/12/91	11:20	11:42	11:17	PST	23.10	4.09	ELV
39	01/31/92	10:32	11:05	10:07	PST	23.60	2.60	STL
40	01/31/92	11:12	11:58	11:40	PST	24.00	4.90	STL
41	02/14/92	10:04	10:46	09:05	PST	24.10	2.60	NOR
42	02/14/92	11:07	11:34	11:03	PST	24.40	4.90	NOR

Table 5. The vertical modified refractivity profile for the radiosonde of 11 October 1990. Time is 11:54 PDT. The gradient through the boundary layer is estimated as 0.1236 M/m.

Height (m)	M-Units
0.00	347.18
197.13	371.54
286.74	322.22
372.76	332.44
422.94	335.45
523.30	348.08
562.72	349.59
1000.00	407.33

Table 6. Analyst interpretation of the surface meteorological measurements made for the second run of 11 October 1990. Estimated range dependent conditions for ranges of 0 (radar site), 5, 10, 15, and 20 km from radar site. The measurement height of 22.0 m corresponds to the F35 site, while the 2.4 m height corresponds to the measurement height on the boat.

Range (km)	Measurement Height (m)	Air Temp (°C)	Sea Temp (°C)	Relative Humidity	Wind Speed (kn)
0	22.0	19.33	20.01	85.25	5.83
5	2.4	21.11	20.77	80.22	4.41
10	2.4	20.99	21.53	78.60	4.02
15	2.4	20.87	21.52	78.38	3.63
20	2.4	20.76	21.59	78.16	3.23

Table 7. The vertical modified refractivity profile for the radiosonde of 30 January 1991. Time is 10:36 PST. The gradient through the boundary layer is estimated as 0.1025 M/m. This radiosonde was taken from the boat at a range of 2 km from the radar site.

Height (m)	M-Units
0.00	314.25
50.18	325.08
71.68	310.04
232.97	326.58
265.23	331.99
315.41	338.31
358.42	340.71
376.34	339.21
451.61	347.63
483.87	348.53
634.41	367.48
989.25	415.00

Table 8. Analyst interpretation of the surface meteorological measurements made for the outbound run of 30 January 1991 starting at 12:23 PST. Range 0 corresponds to the F35 site, all other ranges are measurements from the boat.

Range (km)	Measurement Height (m)	Air Temp (°C)	Sea Temp (°C)	Relative Humidity	Wind Speed (kn)
0	22.0	14.54	14.97	64.15	7.50
2.5	2.4	14.89	15.15	64.58	3.50
5	2.4	14.65	15.33	66.72	3.50
7.5	2.4	14.91	15.51	68.86	3.50
10	2.4	15.18	15.69	70.48	3.50
12.5	2.4	15.46	15.78	71.32	3.50
15	2.4	15.74	15.82	72.15	3.50
17.5	2.4	16.02	15.85	72.98	3.50

Table 9. Analyst interpretation of the surface meteorological measurements made for the outbound run of 5 December 1990 starting at 12:06 PST. Range 0 corresponds to the F35 site, all other ranges are measurements from the boat.

Range (km)	Measurement Height (m)	Air Temp (°C)	Sea Temp (°C)	Relative Humidity	Wind Speed (kn)
0	22	15.40	14.86	77.60	2.96
2.50	2.4	16.65	14.81	76.56	0.96
5.00	2.4	15.90	15.68	76.50	0.96
7.50	2.4	15.50	15.86	76.43	0.96
10.00	2.4	15.38	15.86	76.37	0.96
12.50	2.4	15.32	15.86	76.31	0.96
15.00	2.4	15.30	15.86	76.24	0.96
17.50	2.4	15.30	15.86	76.18	0.96
20.00	2.4	15.30	15.86	76.11	0.96

Table 10. The vertical modified refractivity profile for a radiosonde of 5 December 1991. Time is 12:02 PST. The gradient through the boundary layer is estimated as 0.2145 M/m. This radiosonde was taken from the boat at a range of 2 km from the radar site.

Height (m)	M-Units
0.00	319.32
96.77	340.08
164.87	326.24
225.81	335.56
290.32	327.44
379.93	333.16
422.94	341.28
548.39	350.60
1000.00	412.26

Table 11. The vertical modified refractivity profile for the radiosonde of 5 December 1991. Time is 12:45 PST. The gradient through the boundary layer is estimated as 0.1907 M/m (heights 50.18 to 168.46 m used in computing the gradient). This radiosonde was taken from the boat at a range of 20 km from the radar site.

Height (m)	M-Units
0.00	333.23
50.18	332.63
168.46	355.19
225.81	356.09
258.06	329.32
326.16	327.82
537.63	351.58
1000.00	413.23

Table 12. Measured detection range (km) for the 4.9-m target.

Seq. No.	File Name MoDaYr.Run	125-dB Threshold	130-dB Threshold	135-dB Threshold	140-dB Threshold
1	101190.00	5.70	12.30	16.90	NaN
2	101190.01	5.70	11.70	17.30	NaN
3	112090.00	NaN	13.70	25.50	NaN
4	112090.01	NaN	13.30	24.70	NaN
6	121190.01	5.90	6.90	15.50	22.30
7	121890.00	5.30	12.90	16.90	20.90
8	121890.01	5.50	13.10	16.50	20.30
9	013091.00	5.30	5.90	17.70	21.70
10	013091.03	5.90	13.10	16.70	21.10
11	013091.06	6.10	11.30	18	NaN
12	013091.07	5.0	11.90	NaN	NaN
13	021391.00	5.50	11.50	15.10	18.50
14	021391.01	5.30	11.70	15.70	18.30
15	030691.00	4.90	9.90	16.10	20.70
16	030691.01	5.50	11.10	17.10	21.90
17	031191.00	5.30	9.10	15.90	21.70
18	031191.01	4.70	10.90	17.10	24.70
19	031491.00	4.70	8.70	14.70	18.70
20	031491.01	5.10	12.30	17.10	24.10
21	043091.00	5.70	13.30	16.90	20.30
22	043091.01	5.70	14.10	18.30	20.90
24	080191.01	5.90	14.30	17.90	22.50
26	080891.01	5.90	13.70	17.30	21.70
28	081591.01	5.90	14.70	18.50	23.10
30	091291.01	5.70	12.90	17.90	NaN
32	101091.01	5.30	13.50	21.30	NaN
34	102491.01	5.90	11.50	17.90	25.10
36	120591.01	6.30	14.50	16.70	20.90
38	121291.01	5.70	13.30	17.70	22
40	013192.01	NaN	NaN	NaN	NaN
42	021492.01	4.50	9.70	15.50	21.10

Table 13. Measured detection range (km) for the 2.6-m target.

Seq. No.	File Name MoDaYr.Run	125-dB Threshold	130-dB Threshold	135-dB Threshold	140-dB Threshold
23	080191.00	8.70	11.30	14.70	19.50
25	080891.00	8.30	11.30	14.70	18.50
27	081591.00	7.30	12.10	15.50	21.10
29	091291.00	7.90	11.50	15.70	20.90
31	101091.00	9.10	12.30	13.90	18.90
33	102491.00	3.90	10.50	15.30	20.30
35	120591.00	8.30	11.30	14.10	17.90
37	121291.00	7.30	10.70	13.50	17.90
39	013192.00	NaN	NaN	NaN	NaN
41	021492.00	5.30	8.90	13.50	16.90

Table 14. Refractive index profile letter designator keyed to the surface layer, range dependency, vertical height spacing, mixed layer M gradient, and surface roughness models used in the construction of the refractive index profile.

Letter Designator	Surface Layer Model	Range Dependency	Fixed Increment or Feature Profile	Height Where Mixed Layer M Gradient is Applied to Profile	Surface Roughness Parameter Z_0
A	LKB	Range Dependent	Incremental (DelZPE)	Not Applied	LKB
B	LKB	Range Dependent	Feature	Not Applied	LKB
C	Modified LKB	Range Dependent	Incremental (DelZPE)	L′	LKB
D	Modified LKB	Range Dependent	Feature	L′	LKB
E	Modified LKB	Range Dependent	Incremental (DelZPE)	L′	Z_0 Fixed to 0.00001
F	Modified LKB	Range Dependent	Feature	L′	Z_0 Fixed to 0.00001
G	Modified LKB	Fixed Site (F35)	Incremental (DelZPE)	L′	Z_0 Fixed to 0.00001
H	Modified LKB	Fixed Site (F35)	Feature	L′	Z_0 Fixed to 0.00001
M	Jeske	Range Dependent	Incremental (DelZPE)	Not Applied	Jeske
N	Jeske	Range Dependent	Feature	Not Applied	Jeske
O	Modified Jeske	Range Dependent	Incremental (DelZPE)	L′	Jeske
P	Modified Jeske	Range Dependent	Feature	L′	Jeske
Q	Modified Jeske	Range Dependent	Incremental (DelZPE)	L′	Z_0 Fixed to 0.00001
R	Modified Jeske	Range Dependent	Feature	L′	Z_0 Fixed to 0.00001
S	Modified Jeske	Fixed Site (F35)	Incremental (DelZPE)	L′	Z_0 Fixed to 0.00001
T	Modified Jeske	Fixed Site (F35)	Feature	L′	Z_0 Fixed to 0.00001

Table 15. Average, median, and variance of difference between measured and predicted radar detection range (km) for propagation loss thresholds of 125 and 130 dB. Radar target height is 4.9 m. Positive average and median values indicate measured detection range exceeds predicted detection range.

Profile Designator	125-dB Propagation Loss Threshold			130-dB Propagation Loss Threshold		
Type	Average	Median	Variance	Average	Median	Variance
Std	-0.10	0.00	0.20	-1.60	-1.20	4.70
A	-0.60	-0.40	0.40	0.80	0.00	12.50
B	-0.50	-0.20	0.40	0.60	0.00	12.30
C	-0.50	-0.20	0.50	1.00	0.20	11.10
D	-0.40	-0.20	0.40	0.90	0.10	11.00
E	-0.40	-0.20	0.40	0.40	-0.10	10.50
F	-0.30	-0.10	0.40	0.30	-0.10	11.30
G	-0.30	0.00	0.30	-1.20	-0.80	4.60
H	-0.20	0.00	0.30	-1.10	0.80	4.80
M	-0.80	-0.50	0.60	0.80	0.60	21.80
N	-0.70	-0.40	0.60	0.90	0.60	21.20
O	-0.80	-0.40	0.80	1.10	1.00	18.80
P	-0.70	-0.40	0.60	1.40	0.60	9.40
Q	-0.60	-0.40	0.50	1.30	0.20	7.90
R	-0.50	-0.20	0.50	1.00	0.20	7.80
S	-0.50	-0.20	0.40	1.10	0.20	9.40
T	-0.40	-0.20	0.40	1.00	0.20	8.30

Table 16. Average, median, and variance of difference between measured and predicted radar detection range (km) for propagation loss thresholds of 135 and 140 dB. Radar target height is 4.9 m. Positive average and median values indicate measured detection range exceeds predicted detection range.

Profile Designator	125-dB Propagation Loss Threshold			130-dB Propagation Loss Threshold		
Type	Average	Median	Variance	Average	Median	Variance
Std	0.80	0.30	5.90	1.80	1.70	3.20
A	-0.30	-2.10	24.10	-2.10	-2.30	4.40
B	-1.40	-2.20	13.00	-2.10	-2.10	3.20
C	0.70	-0.10	20.00	0.00	0.70	4.90
D	-0.40	-0.60	12.20	0.000	0.80	4.20
E	-1.30	-1.00	6.50	-0.40	0.00	4.90
F	-1.30	-1.00	6.80	0.00	0.60	4.00
G	-1.20	-1.40	8.10	-1.10	-0.80	11.10
H	-1.10	-1.40	7.40	-0.90	-0.80	12.00
M	-0.60	-3.20	49.70	5.50	8.60	73.20
N	-0.40	-3.20	50.40	2.90	1.90	61.40
O	0.40	-0.80	38.30	4.00	2.00	28.20
P	0.40	-1.20	39.50	2.30	1.20	31.10
Q	0.10	0.00	29.50	1.20	1.10	14.00
R	-0.30	-1.20	17.70	1.00	1.00	14.90
S	-2.20	-2.60	7.10	-3.10	-2.80	20.50
T	-2.00	-2.60	7.50	-2.80	-2.20	22.40

Table 17. Average, median, and variance of difference between measured and predicted radar detection range (km) for propagation loss thresholds of 125 and 130 dB. Radar target height is 2.6 m. Positive average and median values indicate measured detection range exceeds predicted detection range.

Profile Designator	125-dB Propagation Loss Threshold			130-dB Propagation Loss Threshold		
Type	Average	Median	Variance	Average	Median	Variance
Std	-1.20	-0.60	2.90	0.00	0.20	1.00
A	0.90	0.40	7.40	-1.80	-1.80	1.20
B	0.40	0.00	9.60	-1.80	-1.80	1.40
C	0.10	0.20	3.60	-1.00	-0.80	2.00
D	-0.30	0.00	5.30	-1.00	-0.80	2.00
E	-0.30	0.00	5.40	-0.90	-0.60	1.90
F	-0.80	0.00	3.00	-0.80	-0.60	1.70
G	-0.80	-0.40	3.50	-0.80	-0.40	1.80
H	-0.90	-0.40	3.50	-0.80	-0.40	1.60
M	0.50	0.20	4.90	-1.90	-1.80	1.60
N	0.50	0.40	5.10	-1.80	-1.80	1.60
O	0.60	0.20	6.30	-1.20	-0.80	2.10
P	0.60	0.40	6.40	-1.20	-0.80	2.10
Q	0.60	0.40	6.60	-1.10	-0.60	2.10
R	-0.30	0.00	5.80	-1.00	-0.60	1.80
S	-0.40	-0.40	5.80	-1.10	-0.60	1.70
T	-0.40	-0.40	6.20	-1.00	-0.40	1.80

Table 18. Average, median, and variance of difference between measured and predicted radar detection range (km) for propagation loss thresholds of 135 and 140 dB. Radar target height is 2.6 m. Positive average and median values indicate measured detection range exceeds predicted detection range.

Profile Designator	125-dB Propagation Loss Threshold			130-dB Propagation Loss Threshold		
Type	Average	Median	Variance	Average	Median	Variance
Std	0.60	0.80	0.70	2.50	2.30	2.10
A	-3.30	-3.60	2.00	-1.70	-1.60	0.10
B	-3.10	-3.40	1.90	-2.50	-1.50	3.80
C	-2.00	-1.80	2.60	-1.60	-1.40	3.90
D	-1.80	-1.60	2.60	-1.40	-1.40	3.70
E	-1.40	-1.20	1.90	-1.30	-0.60	5.90
F	-1.20	-1.20	1.60	-1.00	-0.50	4.70
G	-1.20	-1.00	1.20	-0.60	0.20	3.80
H	-1.10	-1.00	1.40	-0.50	0.00	3.70
M	-3.40	-3.80	2.00	-3.40	-3.00	3.00
N	-3.50	-3.80	2.20	-3.40	-2.90	3.30
O	-2.50	-2.20	3.50	-2.20	-2.20	8.10
P	-2.30	-2.00	3.20	-3.10	-2.60	12.30
Q	-2.00	-1.20	3.30	-0.70	-1.00	3.80
R	-1.80	-1.20	2.80	-0.50	-0.80	3.30
S	-2.00	-1.80	1.80	-2.20	-1.60	7.30
T	-1.90	-1.60	1.80	-2.10	-1.60	6.70

Table 19. Variance of the average, variance of the median, and variance of the difference between measured and predicted radar detection range (km) for propagation loss thresholds of 125, 130, 135, and 140 dB. Radar target heights of 4.9 and 2.6 m.

Profile Designator	Variance of Error Over All Four Propagation Loss Thresholds. 4.9-m Target Height			Variance of Error Over All Four Propagation Loss Thresholds. 2.6-m Target Height		
Type	Average	Median	Variance	Average	Median	Variance
Std	1.61	1.11	16.80	2.01	1.58	3.58
A	1.37	2.46	189.15	4.46	4.73	15.05
B	1.74	2.32	82.67	4.81	4.34	28.04
C	0.44	0.14	136.87	1.89	1.47	9.73
D	0.28	0.26	71.91	1.57	1.29	13.14
E	0.54	0.26	44.17	1.14	0.54	17.90
F	0.47	0.34	47.52	0.93	0.51	9.13
G	1.05	0.81	52.52	0.77	0.34	7.84
H	0.82	0.81	55.47	0.73	0.33	7.62
M	7.97	21.20	2075.98	6.75	6.68	9.89
N	2.47	3.59	1689.98	6.83	6.56	11.07
O	4.50	1.45	654.05	3.22	2.59	30.49
P	1.97	0.85	654.04	4.17	2.89	51.73
Q	0.88	0.35	282.23	1.51	0.74	18.32
R	0.59	0.63	149.10	1.14	0.61	13.90
S	3.98	3.67	139.79	2.55	1.58	23.27
T	3.25	2.92	156.76	2.29	1.36	22.45

Table 20. The sorted magnitude of the median difference between the measured and the predicted radar detection range for the 4.9-m target. Sort position 0 indicates which refractivity profile type (letter designation) corresponds to the minimum difference between measured and predicted detection range.

Sort Position	125-dB Threshold	130-dB Threshold	135-dB Threshold	140-dB Threshold	Composite Threshold
0	H	B	Q	E	C
1	G	A	C	F	E
2	Std	F	Std	C	D
3	F	D	D	D	F
4	D	E	O	H	O
5	C	C	F	G	R
6	E	R	E	R	H
7	R	T	R	Q	G
8	B	S	P	P	P
9	T	Q	H	Std	Std
10	S	P	G	N	O
11	Q	N	A	O	B
12	A	M	B	B	A
13	P	J	T	T	T
14	N	G	S	A	N
15	O	O	N	S	S
16	M	Std	M	M	M

Table 21. The sorted magnitude of the variance of the difference between the measured and the predicted radar detection range for the 4.9-m target. Sort position 0 indicates which refractivity profile type (letter designation) corresponds to the minimum difference between measured and predicted detection range.

Sort Position	125-dB Threshold	130-dB Threshold	135-dB Threshold	140-dB Threshold	Composite Threshold
0	Std	G	Std	Std	Std
1	H	Std	E	B	E
2	G	H	F	F	F
3	E	R	S	D	G
4	D	Q	H	A	H
5	F	T	T	E	D
6	B	S	G	C	B
7	A	P	D	G	C
8	T	E	B	H	S
9	S	D	R	Q	R
10	C	C	C	R	T
11	Q	F	A	S	A
12	R	B	Q	T	Q
13	P	A	O	O	P
14	N	O	P	P	Q
15	M	N	M	N	N
16	O	M	N	M	M

Table 22. The sorted magnitude of the median difference between the measured and the predicted radar detection range for the 2.6-m target. Sort position 0 indicates which refractivity profile type (letter designation) corresponds to the minimum difference between measured and predicted detection range.

Sort Position	125-dB Threshold	130-dB Threshold	135-dB Threshold	140-dB Threshold	Composite Threshold
0	F	Std	Std	H	H
1	E	H	H	G	G
2	R	G	G	F	F
3	D	T	F	E	E
4	B	F	E	R	R
5	C	E	R	Q	Q
6	O	R	Q	D	D
7	M	Q	T	C	T
8	H	S	D	T	C
9	G	D	S	S	S
10	Q	C	C	B	Std
11	T	O	P	A	O
12	S	P	O	O	P
13	P	B	B	Std	B
14	A	M	A	P	A
15	N	A	M	N	N
16	Std	N	N	M	M

Table 23. The sorted magnitude of the variance of the difference between the measured and the predicted radar detection range for the 2.6-m target. Sort position 0 indicates which refractivity profile type (letter designation) corresponds to the minimum difference between measured and predicted detection range.

Sort Position	125-dB Threshold	130-dB Threshold	135-dB Threshold	140-dB Threshold	Composite Threshold
0	Std	Std	Std	A	Std
1	F	A	G	Std	H
2	H	B	H	M	G
3	G	H	F	N	F
4	C	M	S	R	C
5	M	N	T	H	M
6	N	F	B	D	N
7	D	S	E	G	D
8	E	G	A	B	R
9	R	R	M	Q	A
10	S	T	N	C	E
11	T	E	C	F	Q
12	O	C	D	E	T
13	P	D	R	T	S
14	Q	O	P	S	B
15	A	P	Q	O	O
16	B	Q	O	P	P

REFERENCES

Anderson, K. D. 1993. "Radar detection of low-altitude targets in a maritime environment: data report," TR 1630, vol. 2, NCCOSC RDT&E Division, San Diego, CA.

Bean, B. R., and E. J. Dutton. 1966. *Radio Meteorology*, National Bureau of Standards Monograph 92 (March).

Barrios, A. E. 1992. "Parabolic equation modeling in horizontally inhomogeneous environments," *IEEE Trans. Ant. and Prop.*, vol. 40, pp. 791–797 (July).

Dockery, G. D. 1988a. "Propagation fade characteristics in low-altitude surface ducts," The Johns Hopkins University/Applied Physics Laboratory, Technical Report, Task 3–1–19 (20 October).

Dockery, G. D. 1988b. "Modeling electromagnetic wave propagation in the troposphere using the parabolic equation," *IEEE Trans. Ant. and Prop.*, vol. 36, pp. 1464–1470 (October).

Gossard, E. E., and R. G. Strauch. 1983. *Radar Observation of Clear Air and Clouds*, New York: Elsevier.

Hitney, H. V., J. H. Richter, R. A. Pappert, K. D. Anderson, and G. B. Baumgartner, Jr. 1985. "Tropospheric radio propagation assessment," *Proc. IEEE*, vol. 73, pp. 265–285 (February).

Hitney, H. V. 1992. "Hybrid ray optics and parabolic equation methods for radar propagation modeling," in *Radar 92*, IEE Conference Publication No. 365, pp. 58–61, Brighton, UK (12-13 October).

Jeske, H. 1973. "State and limits of prediction methods of radar wave propagation conditions over sea," *Modern Topics in Microwave Propagation and Air-Sea Interaction*, A. Zancla, Ed., Reidel Pub., Boston, Massachusetts.

Liu, W. T., K .B. Katsaros, and J. A. Businger. 1979. "Bulk parameterization of air-sea exchanges of heat and water vapor including the molecular constraints at the interface," *Jour. of the Atmos. Sciences*, vol. 36, pp. 1722–1735 (September).

Liu, W. T., and T. V. Blanc. 1984. "The Liu, Katsaros, and Businger (1979) bulk atmospheric flux computational iteration program in FORTRAN and BASIC," Naval Research Laboratory (NRL) Memorandum Rep. 5291 (8 May).

Lumley, J. L., and H. A. Panofsky. 1964. *The Structure of Atmospheric Turbulence*, Interscience Publishers, New York, NY.

Monin, A. S., and A. M. Obukhov. 1954. "Basic regularity in turbulent mixing in the surface layer of the atmosphere," *Trudy Geophys. Inst. ANSSSR*, No. 24, p. 163.

Panofsky, H. A., and J. A. Dutton. 1983. *Atmospheric Turbulence*, John Wiley & Sons, New York, NY.

Paulus, R. A. 1989. "Specification for environmental measurements to assess radar sensors," NOSC TD 1685, Naval Ocean Systems Center, San Diego, CA (November).

Patterson, W. L., C. P. Hattan, H. V. Hitney, R. A. Paulus, A. E. Barrios, G. E. Lindem and K. D. Anderson. 1990. "Engineer's refractive effects prediction system (EREPS) Revision 2.0," NOSC TD 1342, Revision 2.0, Naval Ocean Systems Center, San Diego, CA (February).

Tappert, F. D. 1977. "The parabolic approximation method," in *Wave Propagation and Underwater Acoustics*, J. B. Keller and J. S. Papadakis, Eds., Springer-Verlag, New York, NY.

REPORT DOCUMENTATION PAGE

Form Approved
OMB No. 0704-0188

1. AGENCY USE ONLY *(Leave blank)*	2. REPORT DATE	3. REPORT TYPE AND DATES COVERED
	October 1993	Final: Nov 1993

4. TITLE AND SUBTITLE

RADAR DETECTION OF LOW-ALTITUDE TARGETS IN A MARITIME ENVIRONMENT
Final Analysis

5. FUNDING NUMBERS

PE: 0602435N
AN: DN302214

6. AUTHOR(S)

K. D. Anderson

7. PERFORMING ORGANIZATION NAME(S) AND ADDRESS(ES)

Naval Command, Control and Ocean Surveillance Center (NCCOSC),
RDT&E Division
San Diego, CA 92152-5001

8. PERFORMING ORGANIZATION REPORT NUMBER

TR 1630
Vol. 1

9. SPONSORING/MONITORING AGENCY NAME(S) AND ADDRESS(ES)

Office of Naval Research, Code 453
800 N. Quincy Street
Arlington, VA 22217

10. SPONSORING/MONITORING AGENCY REPORT NUMBER

11. SUPPLEMENTARY NOTES

12a. DISTRIBUTION/AVAILABILITY STATEMENT

Authorized for public release; distribution is unlimited.

12b. DISTRIBUTION CODE

13. ABSTRACT *(Maximum 200 words)*

Results from a unique analytical and measurement effort to assess low-altitude, short-range, radar detection capabilities in an evaporation ducting environment validate propagation model predictions of reduced radar detection ranges within the radio horizon. In addition, discrepancies between measured and predicted radar data demand a close examination of both meteorological data and surface layer theory. At ranges near and beyond the horizon, radar detection crucially depends both on the surface layer refractivity profile and on the adjacent mixed layer refractivity profile. A unified boundary layer model, an empirical model to merge the surface layer with the mixed layer, is described. Other discrepancies, which are thought to be caused either by inadequate surface layer modeling (perhaps the moisture stability function) or by inadequate boundary layer meteorological measurements, suggest the need for improvements in surface layer modeling and the need for new techniques to measure the refractivity structure.

The combination of direct boundary layer (surface and mixed layer) meteorological measurements, remotely sensed radar measurements, and advanced numerical modeling capability provides valuable insight for a better understanding of the atmospheric boundary layer and its effects on the radar detection of low-altitude short-range targets.

14. SUBJECT TERMS

Electromagnetic
Propagation
Atmosphere

15. NUMBER OF PAGES

73

16. PRICE CODE

17. SECURITY CLASSIFICATION OF REPORT	18. SECURITY CLASSIFICATION OF THIS PAGE	19. SECURITY CLASSIFICATION OF ABSTRACT	20. LIMITATION OF ABSTRACT
UNCLASSIFIED	UNCLASSIFIED	UNCLASSIFIED	SAME AS REPORT

21a. NAME OF RESPONSIBLE INDIVIDUAL	21b. TELEPHONE *(include Area Code)*	21c. OFFICE SYMBOL
K. D. Anderson	(619) 553–1420	Code 543

INITIAL DISTRIBUTION

Code 0012	Patent Counsel	(1)
Code 02712	Archive/Stock	(6)
Code 0274B	Library	(2)
Code 54	J. H. Richter	(1)
Code 543	R. A. Paulus	(1)
Code 543	K. D. Anderson	(25)
Code 7501	B. F. Summers	(1)
Code 755	R. J. Dinger	(1)

Defense Technical Information Center
Alexandria, VA 22304-6145 (4)

NCCOSC Washington Liaison Office
Washington, DC 20363-5100

Center for Naval Analyses
Alexandria, VA 22302-0268

Navy Acquisition, Research and Development
Information Center (NARDIC)
Arlington, VA 22244-5114

GIDEP Operations Center
Corona, CA 91718-8000

NCCOSC Division Detachment
Warminster, PA 18974-5000

Naval Surface Warfare Center
Dahlgren, VA 22448-5000 (2)

Naval Research Laboratory
Washington, DC 20375-5000 (2)

Johns Hopkins University
Laurel, MD 20723-6099

University of Colorado
Boulder, CO 80309

Codar Ocean Sensors, Ltd.
Mountain View, CA 94039-1087

SWL
Albuquerque, NM 87106

TSC
Silver Springs, MD 20904